Modelling coarse and giant desert dust particles

Eleni Drakaki[1,2], Vassilis Amiridis[1], Alexandra Tsekeri[1], Antonis Gkikas[1], Emmanouil Proestakis[1], Sotirios Mallios[1], Stavros Solomos[3], Christos Spyrou[1], Eleni Marinou[1,4], Claire L. Ryder[5], Demetri Bouris[6], and Petros Katsafados[2]

[1]IAASARS, National Observatory of Athens, Athens GR-15236, Greece
[2]Harokopion University of Athens (HUA), Department of Geography, Athens GR-17671, Greece
[3]Academy of Athens, Research Centre for Atmospheric Physics and Climatology, Athens GR-10679, Greece
[4]Institut für Physik der Atmosphäre, Deutsches Zentrum für Luft- und Raumfahrt, Oberpfaffenhofen, Germany
[5]University of Reading, Department of Meteorology, Reading, RG6 6BB, UK
[6]National Technical University of Athens, School of Mechanical Engineering, Athens, GR-15780, Greece

Correspondence to: Eleni Drakaki (eldrakaki@noa.gr)

Abstract. Dust particles larger than 20 μm in diameter have been regularly observed to remain airborne during long-range transport. In this work, we modify the parameterization of the mineral dust cycle in the GOCART-AFWA dust scheme of WRFV4.2.1, to include also such coarse and giant particles, and we further discuss the underlying misrepresented physical mechanisms which hamper the model in reproducing adequately the transport of the coarse and giant mineral particles. The initial particle size distribution is constrained by observations over desert dust sources. Furthermore, the Stokes' drag coefficient has been updated to account realistic dust particles sizes ($Re < 10^5$). The new code was applied to simulate dust transport over Cape Verde in August 2015 (AER-D campaign). Model results are evaluated against airborne dust measurements and the CALIPSO-LIVAS pure dust product. The results show that the modelled lifetimes of the coarser particles are shorter than those observed. Several sensitivity runs are performed by reducing artificially the particles' settling velocities in order to compensate underrepresented mechanisms, such as the non-spherical aerodynamics, in the relevant parameterization schemes. Our simulations reveal that particles with diameters of 5.5-17 μm and 40-100 μm are better represented under the assumption of a 80% reduction in the settling velocity (UR80) while particles with sizes ranging between 17μm and 40 μm are better represented in a 60% reduction in settling velocity (UR60) scenario. The overall statistical analysis indicates that the best agreement with airborne in-situ measurements downwind (Cape Verde) is achieved with a 40% reduction in settling velocity (UR40). Moreover, the UR80 experiment improves the representation of the vertical structure of the dust layers as those are captured by the CALIPSO-LIVAS vertically-resolved pure dust observations. The current study highlights

29 the necessity of upgrading the existing model parameterization schemes of the dust life-cycle components towards improving

30 the assessment of the dust-related impacts within the Earth-Atmosphere system.

1 Introduction

32   Dust is the most prominent contributor to the global aerosol burden, in terms of dry mass, and it ranks second in

33 aerosol emissions (Gliß et al., 2021; Huneeus et al., 2011; Textor et al., 2006). The major sources of dust are situated across

34 the "dust belt" (Prospero et al., 2002) stretching in the Northern Hemisphere hosting deserts and erodible soils (e.g.,Goudie

35 and Middleton, 2006), that are prone to windblown dust. Most of the global dust budget comes from the Sahara Desert,

36 followed by deserts in the Middle East and Asia. (Ginoux et al., 2012; Huneeus et al., 2011; Kok et al., 2021; Li and Osada,

37 2007). Spatially more limited desert regions in the Southern Hemisphere emit lower amounts of mineral particulate matter

38 (Ginoux et al., 2012; Huneeus et al., 2011; Kok et al., 2021; Li and Osada, 2007), and less than 5% comes from high-latitude

39 sources (Bullard et al., 2016).

40   Dust particles act as ice nuclei (IN) on cold cloud processes (Marinou et al., 2019; Solomos et al., 2011) and when

41 mixed or coated with hygroscopic material, they can affect warm cloud processes (Twohy et al., 2009) and serve as cloud

42 condensation nuclei (CCN). Dust particles rich in key micronutrients such as iron (Fe) and phosphorus (P) affect

43 biogeochemical processes in marine and terrestrial ecosystems (Jickells et al., 2005; Okin et al., 2004; Stockdale et al., 2016;

44 Tagliabue et al., 2017) and disrupt the carbon cycle (Jickells et al., 2014) after their wet and dry deposition. Severe dust

45 episodes can affect aviation and telecommunications (Harb et al., 2013; Weinzierl et al., 2012; Nickovic et al., 2021), human

46 health (e.g., Du et al., 2016; Giannadaki et al., 2014) and solar energy production (Kosmopoulos et al., 2018).

47   Apart from the dust load intensity, the size of the suspended mineral particles plays a determinant role on the related

48 impacts on weather and climate, among others. Larger dust particles act more efficiently as CCN (Petters and Kreidenweis,

49 2013) and IN (Diehl et al., 2014) altering cloud microphysical processes and subsequently the hydrological cycle. Recent

50 studies suggest that coarser dust aerosols are more effective absorbers of the incoming solar radiation, enhancing atmospheric

51 warming (Mahowald et al., 2014; Ryder et al., 2019). Therefore, it is imperative to represent realistically the dust particle size

52 distribution (PSD) facilitating a thorough investigation on the dust transport processes and the dust-induced impacts.

53   Airborne dust particles has been observed to sizes up to 300 μm, whereas even larger particles with diameters up to

54 450 μm have been recorded from in situ deposition measurements acquired at buoys mounted across the Tropical Atlantic

55 Ocean (van der Does et al., 2018). Dust particles are usually divided into three different modes (fine, coarse and giant) without

56 strictly defined bounds of their sizes (Goudie, 2014; Knippertz and Stuut, 2014). According to Ryder et al. (2019), the fine

57 mode represents dust particles with $D \leq 2$ μm, the coarse mode those with diameters between 2 μm and 20 μm, and the giant

58 mode particles with $D \geq 20$ μm. A recent study (Ryder et al., in preparation) suggests that the above modes can be further

59 descritized into four categories, namely fine ($D < 2.5$ μm), coarse (2.5-10 μm), super-coarse (10-62.5 μm), and giant ($D > 62.5$

60 μm).

The existence of dust particles larger than 20 μm in diameter was already demonstrated in the 1970s based on measurements in the Caribbean (Prospero et al., 1970). Nevertheless, these sizes were neglected in atmospheric dust models since giant particles were assumed to be rare. This assumption has been disproved in recent decades by a large number of airborne campaigns equipped with state-of-the-art in situ and remote sensing instruments. Specifically, in the framework of the SAMUM1 (Weinzierl et al., 2009) and SAMUM2 (Liu et al., 2018) experimental campaigns it has been justified that above sources dust aerosols up to 40 μm in diameter were recorded in 20% of the identified dust layers, while over Cape Verde mineral particles up to 30 μm in diameter were measured (Weinzierl et al., 2011). This reduction of dust particle sizes, along the transport pathway, is attributed to the gravitational settling. Similar findings were reported in the FENNEC campaign (Ryder et al., 2013b) with mean effective particle diameters ranges of 22 to 28 μm and 15 to 18 μm for fresh and aged dust, respectively. During the AER-D campaign, in the Saharan outflow zone near Cape Verde and the Canary Islands, mineral particles with diameters larger than 20 μm were systematically recorded, while in 36% of the studied cases, particles with diameters larger than 40 μm recorded (Ryder et al., 2018). Dust particles with diameters of 10 to 30 μm were detected during the SALTRACE campaign in Barbados (Weinzierl et al., 2017), revealing that they were suspended far away from their sources at about 2000 km more than what would be expected from the Stokes' theory (Weinzierl et al., 2017). Atmospheric dust models are the optimal tool to simulate the components of the dust cycle and therefore to study the dust-related effects. However, the state-of-the-art atmospheric dust models are characterized by inherent limitations in accounting for realistic emission and transport dust size distributions (Huang et al., 2020; Kok, 2010; Mahowald et al., 2014). To overcome these model drawbacks, it is needed to extend the PSD towards the giant particles size spectrum in order to shed light on the processes that sustain larger dust aerosols in the atmosphere for longer periods than expected.

Ginoux, (2003) modeled dust aerosols up to 70 μm in diameter using the Global Ozone Chemistry Aerosol Radiation and Transport (GOCART) model and examined the effects of non-sphericity assuming randomly oriented ellipsoidal particles. His results showed that the reduction of the settling velocity results in a better agreement with observations when the aspect ratio is equal or greater than 5. The new modeled particle size distributions (PSDs) were in generally better agreement with the AERONET observations, although the PSDs were significantly underestimated for diameters near 10 μm. The aspect ratio of 5 results in a reduction in settling velocity of about 45% for particles with sphere volume-equivalent diameters near 10 μm and 60% for particles with sphere-volume-equivalent diameters near 30 μm. Maring et al. (2003) applied a simple empirical model and suggested that an upward velocity of 0.0033 ms^{-1} (0.33 cm s^{-1}) is required to accurately predict PSD changes during transport. Although their comparisons were limited to sizes up to 25 μm, they pointed out that unknown or not well-known processes counteract gravity settling. Possible mechanisms which can interpret the aforementioned findings are (i) vertical mixing within the Saharan air layer during the day (Gasteiger et al., 2017), (ii) the lower settling velocities of non-spherical dust particles (Huang et al., 2020; Mallios et al., 2022), (iii) the underrepresented meteorological conditions (O'Sullivan et al., 2020), (iv) the unresolved turbulence (Gu et al., 2021), (v) the electrification of dust (Daskalopoulou et al., 2021; Mallios et al., 2021a; Mallios et al., 2022; Joseph R. Toth III et al., 2020; Renard et al., 2018; Nicoll et al., 2011) and (vi) the numerical errors that perturb the mass balance (Ginoux, 2003).

95   In this work, we demonstrate for the first time a method for incorporating coarse and giant desert dust particles (D >
96   20 μm, following the definition of the dust modes proposed in Ryder et. al, (2019), into the Advanced Research Weather
97   version of the Weather Research and Forecasting (WRF-ARW) model in conjunction with the GOCART (Ginoux, 2003)
98   aerosol model and the Air Force Weather Agency (AFWA) dust emission scheme (LeGrand et al., 2019) (WRF-GOCART-
99   AFWA model). After pinpointing that the model quickly deposits coarse and giant dust particles, we investigate the reasons
100   behind those findings: We use sophisticated in situ PSD measurements to initialize the model over the sources and to evaluate
101   the simulated PSD over the receptor areas. We also use pure-dust spaceborne retrievals to assess the model performance in
102   terms of reproducing the vertical structure of the dust layers. In addition, we perform a series of sensitivity tests by reducing
103   the settling velocity of mineral particles in the model and we investigate the concomitant effects on dust fields. The article is
104   organized as follows: In Sect. 2, we describe the methodology in terms of the changes we made to the code of WRF-GOCART-
105   AFWA, the setup of the model and the experiments performed, and the observational data we used for model validation. The
106   results of our work are presented in Sect. 3, Sect. 4 contains the discussion and Sect.5 the summary and the conclusions of this
107   work.

2 Model and Data

2.1. WRF-GOCART-AFWA model

110   In our numerical experiments to study the transport of coarse and giant dust aerosols, we use the WRF-ARWv4.2.1
111   model coupled with the GOCART aerosol model and the AFWA dust emission scheme (LeGrand et al., 2019). The current
112   version of the WRF-GOCART-AFWA model accounts for giant dust particles in the calculated dust emission fluxes (up to
113   125 μm) and assumes that the transported dust particles are up to 20 μm in diameter. To extend the transport PSD to coarser
114   and giant mineral particles, we implemented several developments in the standard WRF-GOCART-AFWA model, which are
115   discussed in Sect. 2.1.1 and 2.1.2. Figure 1 shows a sketch of the workflow: the first three steps refer to the implemented
116   modifications in the standard WRF-GOCART-AFWA code: In **step 1**, we establish the definition of a prescribed PSD for the
117   emitted dust particles at the source based on in situ reference measurements, and we distribute the total emitted dust
118   accordingly; in **step 2**, we define five size ranges (five model size bins) for the transported PSD covering dust particle sizes
119   (in diameter) spanning from 0.2 μm to 100 μm (Sect. 2.1.1); in **step 3**, we implement an updated drag coefficient that applies
120   to the sizes of the entire range of Aeolian dust PSD (Sect. 2.1.2). These code upgrades are integrated into the new WRF-L
121   model. Table 1 shows the properties of the size bins in the standard WRF-GOCART-AFWA code and the size classes defined
122   in the new WRF-L code. At **step 4** we perform model experiments and validate the model results using different model
123   configurations against observations (Sect. 2.2), as described in detail in Sect. 3.

2.1.1 Dust size distribution

In observational studies of non-spherical particles, it is customary to describe their size in terms of spherical volume equivalent diameter. Here, to describe particles' sizes distributed within the five size bins of the WRF-L model, we use the sphere-volume-equivalent effective diameter (D_{eff}), which is more relevant to the optical properties of the particles (Hansen and Travis, 1974). In this way, we simplify the comparison between the model calculations and the observations of the optical properties of the particles (e.g., dust optical depth). The D_{eff} in (μm) of each size bin is calculated as shown in Eq. 1, and is provided in Table 1.

$$D_{eff} = \frac{\int_{D_{lo,k}}^{D_{u,k}} D^3 \cdot \frac{dN}{dD} \cdot dD}{\int_{D_{lo,k}}^{D_{u,k}} D^2 \cdot \frac{dN}{dD} \cdot dD},\tag{1}$$

Where D is the particle diameter in (m) and $\frac{dN}{dD}$ is the particle number size distribution in number of particles per m^3. The parameters at each size bin k are listed in Table 1. Henceforward, references about the size of the particle correspond to particle volume equivalent effective diameter, unless mentioned otherwise.

In the default GOCART-AFWA dust emission scheme of WRF, the total emitted vertical dust flux is estimated at each grid point prone to dust emission, when favorable conditions are met. The dust flux is then distributed over five transport size bins, based on the fragmentation theory of Kok, (2011), bounded to diameters up to 20 μm. Since our goal is to consider larger dust particles than those commonly used in the current atmospheric dust models, we redefine the five transport model bins including particles with diameters up to 100 μm (Table 1). We rely on prescribed PSD for the emitted dust particles at the source based on the airborne in situ measurements acquired during the FENNEC campaign of 2011 (Ryder et al., 2013a). More specifically, for the freshly uplifted dust we use the mean PSD at the lowest available height (i.e., 1km), obtained by averaging profile measurements above the Sahara (Mauritania and Mali), hereafter called the "observed FENNEC-PSD", which is shown in Fig. 2(a) with red squares. Figure 2a shows also the "fitted FENNEC-PSD" (solid red line), which is the fit of the "observed FENNEC-PSD", using five lognormal modes (Table 4). In Sect. 2.2.1 more information is provided on the derivation of the mean "observed FENNEC-PSD", including also the description of the FENNEC 2011 campaign, the in-situ instrumentation used and the processing of the acquired data. Based on the FENNEC-PSD we calculate the mass fraction ($k_{factors}$) distributed among the redefined transport model size bins in Eq. 2. The weighting factors $k_{factors}$ are shown in Fig.2(b).

$$k_{factors} = \frac{\int_{D_{lo,k}}^{D_{u,k}} \frac{1}{D} \frac{dV}{dlnD} \cdot dD}{\int_{D_{lo,k_{min}}}^{D_{u,k_{max}}} \frac{1}{D} \frac{dV}{dlnD} \cdot dD},\tag{2}$$

153 Where D is the particle diameter, $\frac{dV}{dlnD}$ is the volume size distribution in $\mu m^3 cm^{-3}$, $D_{lo,k}$ and $D_{u,k}$ are the margins of each size

154 bin k in μm.

2.1.2 Updated gravitational scheme

156 In the GOCART-AFWA dust scheme of WRF, the forces acting on a dust particle moving along the vertical direction

157 are the gravitational force F_g and the aerodynamic drag force F_{drag}, which are mathematically expressed in Eq.3 and Eq.4,

158 respectively.

$$F_g = \rho_p \cdot V_p \cdot g, \tag{3}$$

$$F_{drag} = \frac{1}{2} \cdot \frac{C_D}{C_{cun}} \cdot A_p \cdot \rho_{air} \cdot u_{term}^2, \tag{4}$$

163 Where ρ_p stands for particle density in kgm^{-3}, g corresponds to the gravitational acceleration in ms^{-2}, $V_p = \frac{1}{6} \cdot \pi \cdot D_{eff}^3$ is the

164 particle volume in m^3 and $A_p = \frac{\pi}{4} \cdot D_{eff}^2$, is the particle's projected area normal to the flow in m^2, ρ_{air} is the air density in

165 kgm^{-3}. and D_{eff} represents the particles' diameter in m for each model size bin (assuming spherical particles, as defined in

166 Sect. 2.1.1). C_D is the aerodynamic drag coefficient (unit less) and C_{cun} is the slip correction to account for slip boundary

167 conditions (Davies, 1945) and it is expressed as a function of the air mean free path (λ, in meters) (Eq. 5):

$$C_{cun} = C_{cun}(\lambda) = 1.0 + \frac{2 \cdot \lambda}{D_{eff}} [1.257 + 0.4 \cdot e^{\frac{-1.1 \cdot D_{eff}}{2 \cdot \lambda}}], \tag{5}$$

171 The constant velocity that a particle builds up falling vertically within the Earth's atmosphere, is defined as the terminal settling

172 velocity u_{term}, and it can be estimated by solving the 1-D equation of motion at the steady state limit, where net force is

173 assumed to be equal to zero:

$$\rho_p \cdot V_p.g = \frac{1}{2} \cdot \frac{C_D}{C_{cun}} \cdot A_p \cdot \rho_{air} \cdot u_{term}^2, \tag{6}$$

177 In the default GOCART-AFWA dust scheme the drag coefficient is given by Stokes' Law and is defined as:

$$C_D = \frac{12}{Re}, \tag{7}$$

180 Where Re is the Reynold's number (unit less) given by the following equation as a function of the particle volume equivalent

181 effective diameter D_{eff}:

182

183 $$Re = \frac{\rho_{air} \cdot u_{term} \cdot D_{eff}}{2 \cdot \mu},\qquad(8)$$

184

185 Where μ is the air dynamic viscosity in $\frac{kg}{m \cdot s}$ defined as a function of air temperature T in K by the following equation (Hilsenrath,

186 1955; United States Committee on Extension to the Standard Atmosphere., 1976):

187

188 $$\mu = \frac{\beta \cdot T^{\frac{3}{2}}}{T+S},\qquad(9)$$

189

190 where S is the Sutherland constant which equal to $110.4\,K$ and β is a constant which equals to $1.458 \cdot 10^{-6}\,kg \cdot m^{-1} \cdot s^{-1} \cdot$

191 $K^{-1/2}$.

192 and the air mean free path is expressed as:

193 $$\lambda = \frac{1.1 \cdot 10^{-3} \cdot \sqrt{T}}{P}\qquad(10)$$

194 Where T is the air temperature in K and P the air pressure in hPa.

195

196 The slip-corrected drag coefficient of the Stokes' Law ($\frac{12}{Re \cdot C_{cun}}$) is valid only for Re <<1, thus it is not representative

197 for particles with D_{eff} larger than ~10 μm. Therefore, an adaptation of the drag coefficient is needed in order to be valid for

198 higher Re values (i.e., 0<Re<16), since in our work dust particles with diameters larger than 20 μm are considered. To realize,

199 we use the drag coefficient C'_D (Eq. 11), proposed by Clift and Gauvin, (1971):

200

201 $$C'_D = \frac{12}{Re} \cdot (1 + 0.2415 \cdot Re^{0.687}) + \frac{0.42}{1+\frac{19019}{Re^{1.16}}},\ for\ \ Re < 10^5\qquad(11)$$

202

203 Mallios et al., (2020) used the same C'_D as a reference for the development of a drag coefficient for prolate ellipsoids, as more

204 suitable for $Re < 10^5$. The departures between the drag coefficients given by Stokes and Clift and Gauvin (1971) become

205 more evident for increasing particles' sizes. More specifically, the drag coefficient given by Clift and Gauvin (1971) can be

206 up to 2 times higher than those of the Stokes' Law for coarse and giant particles (Fig. S1).

207 In the default WRF code the slip correction is applied unconditionally for all the Re values, probably without affecting

208 the solution significantly due to the small particle sizes ($D_{eff} < 20\,\mu m$). However, in our work a condition is required for

209 applying the slip correction only in the Stokes' regime (e.g. Re < 0.1, Mallios et. al, 2020). Hence, we apply the bisection

210 method to calculate the terminal velocity for each model size bin using the revised drag coefficient and, at first, ignoring the

211 slip correction. When the solution lies in the Stokes' regime (e.g. Re < 0.1), we recalculate the settling velocity using the

212 corrected drag coefficient $C'_{D,slip} = \frac{C'_D}{C'_{cun}}$, where $C'_{cun} = C_{cun}(\lambda')$ with λ' the mean free path obtained by (Jennings, 1988):

213

214 $$\lambda' = \sqrt{\frac{\pi}{8}} \cdot \frac{\frac{\mu}{0.4987445}}{\sqrt{P\rho_{air}}}, \quad (12)$$

2.1.3 Model experiments

216 Using the WRF-L code, we first run the CONTROL experiment. Our simulation period coincides with the AER-D

217 experimental campaign (29/7 - 25/8/2015) for a domain bounded between the 1.42^{o}N and 39.99^{o}N parallels and stretching

218 between the 30.87^{o}W and 46.87^{o}E meridians (Fig. 3). The simulation area encompasses the major Saharan also including the

219 downwind areas in the eastern Tropical Atlantic. We use an equal-distance grid with a spatial grid spacing of 15 km x 15 km

220 consisting of 550 × 300 points whereas in vertical, 70 vertical sigma pressure levels up to 50 hPa are utilized (defined by the

221 model). The simulation period consists of nine 84-hour forecast runs, which are initialized at 12 UTC, using the 6-hour Global

222 Forecast System Final Analysis (GFS - FNL) reanalysis product, available at a 0.25^{o}x0.25^o spatial grid spacing. The sea surface

223 temperatures, acquired by the NCEP daily global SST analysis (RTG_SST_HR), are updated every six hours along with the

224 lateral boundary conditions. Topography is interpolated from the 30-sec Global Multi-resolution Terrain Elevation Data 2010

225 (GMTED2010, Danielson and Gesch, (2011)). Land use is defined based on the Moderate-resolution Imaging

226 Spectroradiometer (MODIS) observational data, modified by the University of Boston (Gilliam and Pleim, 2010). From each

227 84-hours cycle, the first 12 hours are discarded due to model spin up. Likewise, the first week of the simulation served as a

228 spin-up run for the accumulation of the background dust loading and it is excluded from the analysis. The simulation runs are

229 performed in a dust-only mode, neglecting the radiative feedback from aerosols. We scale the dust source strength, by tuning

230 the empirical proportionality constant in the horizontal saltation flux equation (in eq. 10 in LeGrand et al., (2019)) in order to

231 obtain the best match between the modeled DOD and the AERONET AOD (RMSE=0.34, bias=-0.07) acquired at 8 desert

232 stations: Banizoumbou, Dakar, El_Farafra, Medenine- IRA, Oujda, Tizi_Ouzou, Tunis_Carthage, Ben_Salem). Note that we

233 take into account only AERONET records when AODs are higher than 0.2 (Version 3.0, Level 1.5, Giles et al., 2019; Sinyuk

234 et al., 2020) and the Angstrom exponent is lower than 0.75. The tuning constant is equal to 3 and is applied throughout the

235 model domain. The complete configuration options for the run are listed in Table 2. The resolution applied in this study (15km

236 grid spacing) is adequate for the scale of phenomena we want to study, improves the representation of topography and increases

237 the accuracy of the reproduced weather and dust fields compare to coarser resolution such as used in global datasets (e.g. 0.5

238 deg GFS) (Cowie et al., 2015; Basart et al., 2016; Roberts et al., 2017; Solomos et al., 2018). WRF-Chem solver uses a 5th-

239 order horizontal advection scheme and a 3-rd order vertical advection scheme to solve the scalar conservation equation, along

240 with the 3-rd order Runge-Kutta time integration scheme (Grell et al., 2005). The use of such high-order advective schemes

241 eliminate the numerical errors of diffusion in the code. We should note though that in the deposition parameterization of

GOCART-AFWA dust scheme the vertical advection of the losses due to the gravitational settling is solved by a first order explicit scheme, which is notoriously too diffusive (Versteeg and Malalasekera, 2007) and thus it can possibly induce numerical errors in the mass conservation (Ginoux, 2003). A series of additional sensitivity runs has been performed aiming to resemble possible mechanisms (misrepresented or even absent in the model) counteracting gravitational settling towards reducing the differences between the CONTROL run calculations and the in-situ observations (shown in Sect. 3.4). To be more specific, we gradually reduced (with an incremental step of 20%) the settling velocity by up to 80%, with the corresponding runs named as URx (x corresponds to the reduction in percentage terms). Under such theoretical conditions, it is expected that the giant dust particles will be suspended for longer periods and that they will be transported at larger distances than the current state-of-the-art models simulate, failing to reproduce what is observed in the real world. Based on these sensitivity experiments, we defined a constant (by percentage) relevant reduction of the particles' settling, which in its absolute value varies with size. Therefore, it is more similar to the effects that are related to aerodynamic forces due to the non-spherical shape and the orientation of the suspended dust particles (Ginoux, 2003; Loth, 2008; Zastawny et al., 2012; Shao et al., 2017; Sanjeevi et al., 2018; Mallios et al., 2020). Finally, the full list of the performed experiments is given in Table 3.

2.1.4 Dust extinction coefficient

For the evaluation of the model mid-visible (550 nm) dust extinction profiles the corresponding products from the Lidar climatology of Vertical Aerosol Structure for space-based lidar simulation studies (LIVAS) dataset is used as reference. For the spatiotemporal matching between the modelled and the observed dust extinction, we first project the two datasets onto a common horizontal grid, by converting the model outputs from their native horizontal grid spacing (15 km x 15 km) to the structured $1°x1°$ equal lat-lon grid of LIVAS. The model extinction coefficient for each size bin k ($EC_{550,k,n,l}$) is then calculated at each grid cell n and within each model level l, as shown in Eq.13.

$$EC_{550,k,l,n} = \sum_1^k \frac{3}{2\rho_{,k}D_{eff,k}} M_{n,k,l}Q_{ext550,k}, \tag{13}$$

where $M_{n,k,l}, \rho_k, D_{eff,k}$ and $Q_{ext550,k}$ are the grid cell dust mass concentration in g/m³, the particle density in g/m³, the effective diameter in m, and the extinction efficiency factor at 550 nm, of size bin k.
$Q_{ext550,k}$ is calculated using the Mie scattering code (Mie, 1908), considering spherical dust particles, and a refractive index of 1.55 + i0.005, which is representative of dust (e.g. Dubovik et al., 2002). Although the extinction coefficient values for spherical particles may be different from the extinction coefficient values of the dust particles, which have irregular shapes, to our knowledge there is no data available for the extinction coefficient of the latter. The extinction coefficient values of spheroidal shapes, commonly used as a proxy of the dust shapes, are not substantially different compared to the spherical particles (Tsekeri et al., 2022), at least when considering the aspect ratios measured for dust particles in Sahara (Kandler et al., 2009). For simplifying the computations, we assume that the particles in each size bin have the same size (i.e. $D_{eff,k}$), and thus

274 the same $Q_{ext550,k}$. In vertical, the fine resolution LIVAS dust extinction coefficient is rescaled (averaging) to match the model

275 layers vertical margins. In the time dimension, the model outputs at the closest lead times to the satellite overpass are selected.

2.2 Observational datasets

2.2.1 Airborne in situ observations

278   During the FENNEC field campaign in 2011 (Ryder et al., 2013b, 2013a) and the AER-D field campaign in 2015

279 (Ryder et al., 2018, 2019), airborne in situ observations were collected with the FAAM BAE research aircraft. In this study

280 we use size distributions from the FENNEC field campaign, aquired during aircraft profiles over the Sahara (Mauritania and

281 Mali), as described in Ryder et al. (2013a). We select size distributions from "freshly uplifted dust" cases, when dust particles

282 are in the atmosphere for less than 12 h. Additionally, from these profiles we use data from the lowest available altitude,

283 centered at 1km, covering altitudes between 0.75 to 1.25km. The derived PSD is depicted in Fig.2(a), hereafter referred to as

284 the "observed FENNEC-PSD". Error bars in Fig.2(a) indicate the standard deviation of the observed values across the profiles

285 and altitudes we used. The instrumentation for those measurements was the Passive Cavity Aerosol Spectrometer Probe

286 (PCASP, 0.13-3.5 μm), the Cloud Droplet Probe (CDP, 2.9-44.6 μm), using light scattering measurements and assuming a

287 refractive index (RI) of 1.53-0.001i (which is constant with particle size), spherical shape for the particles, and using Mie

288 calculations to convert from optical to geometric diameter, as well as the Cloud Imaging Probe (CIP15, 37.5-300 μm)). The

289 instruments and data processing are described in Ryder et al. (2013a). The midpoint size bin diameters do not overlap, though

290 there is some overlap in bin edges between the instruments. A fit on the observations is provided in Figure 2a (the "fitted

291 FENNEC-PSD" with solid red line), which is used in the parameterization of the emitted dust, as described in Section 2.1.1,

292 to modify the GOCART-AFWA dust scheme in WRF.

293   We also use PSD observations during horizontal flight legs at a constant height (referred either as RUNs or flight

294 segments) over the Atlantic Ocean during AER-D. We use measurements taken with PCASP (D =0.12-3.02 μm) for fine dust

295 particles. For the coarse and giant mode of dust we used measurements from CDP (D=3.4-20 μm, although CDP measurements

296 availability extends up to 95.5 μm as it is explained below) and the two-dimension Stereo probe (2DS, D = 10–100 μm -

297 although the instrument measures up to 1280 μm few particles larger than 100μm were detected). For the light scattering

298 techniques of PCASP and CDP, a RI = 1.53-0.001i is assumed for the conversion of the optical to geometric diameter (as in

299 FENNEC 2011 campaign). CDP observations extend up to the size of 95.5 μm, thus data from CDP and 2DS partly overlap in

300 their size range. Since 2DS observations are more reliable in the overlapping size range, we used the CDP observations for

301 particles with sizes up to 20 μm. Also, 2DS-XY observations are preferred over the 2DS-CC, since they better represent the

302 non-spherical particles. A more detailed description of the in-situ instruments and the corresponding processing of the data

303 acquired during the AER-D campaign is included in Ryder et al., (2018). The error bars represent the total (random and

304 systematic) measurement error due to the counting error, the discretization error, the uncertainties in the sample area and the

305 uncertainties in the bin size due to Mie singularites (Ryder et al., 2018). All PSD measurements are at ambient atmospheric
306 conditions. The locations of the flights of AER-D used in this study are depicted in Fig.3.

2.2.2 LIVAS product

308 For the validation of the vertical distribution of dust from the model (see Sect. 3.5), we utilize the pure-dust profiles
309 provided by the LIVAS dataset, originally presented in Amiridis et al. (2013; 2015) and updated in Marinou et al. (2017). The
310 LIVAS pure-dust product is a global dataset, covering the period between 06/2006 and 05/2020, and is provided a) on per-
311 granule level with similar resolution to the original Cloud-Aerosol Lidar and Infrared Pathfinder Satellite Observations
312 (CALIPSO) L2 profile products (i.e., 5 km horizontal and 60 m vertical), and b) as a global three-dimensional database of
313 monthly-mean averaged profiles of aerosol properties, on a uniform horizontal grid spacing of $1° × 1°$. LIVAS was developed
314 applying the dust-separation technique described in Tesche et al., (2009) on the CALIPSO level 2 version 4 products (Winker
315 et al., 2009). The LIVAS pure-dust product has been used to a variety of dust-oriented studies including the investigation of
316 the dust sources and the seasonal transition of the dust transport pathways (Marinou et al., 2017; Proestakis et al., 2018); the
317 evaluation of the performance of atmospheric and dust transport models (e.g. Tsikerdekis et al., 2017; Solomos et al. 2017;
318 Georgoulias et al., 2018; Konsta et al., 2018), the evaluation of new satellite-based products (e.g. Georgoulias et al., 2016;
319 Chimot at al. 2017; Georgoulias et al., 2020; Gkikas et al., 2021), and on dust assimilation experiments (Escribano et al., 2021).
320 Herein, the LIVAS pure-dust extinction product is used for the assessment of the simulated dust vertical patterns. In the
321 geographical region of our study, the uncertainty of the product is estimated to be less than 20% in altitudes up to 6km (Marinou
322 et al. 2017).

3 Results

3.1 Settling Velocities

325 Figure 4 shows the altitude profiles of the settling velocities for each size bin from the CONTROL run, averaged over
326 the simulation domain, and the period of interest. Settling velocity is increases for larger mineral particles. The terminal
327 velocities for particles within bin 5 are two orders of magnitude higher than those in bin 2 and bin 3, and one order of magnitude
328 with respect to bin 4. An altitude dependency, regulated by the thermodynamic state of the atmosphere, of the terminal
329 velocities is also apparent in Figure 4, showing that they increase with height due to the reduction either of temperature or air
330 density (Eqs. 9 and 13) For the CONTROL run the average settling velocities near the surface are lower by approximately
331 10% than those at 6 km height, and this non-negligible reduction can be critical, particularly for coarser and giant particles
332 where velocities are higher.

3.2 Dust above the sources

In Fig. 5 we present how the PSD varies with height above an emission point (latitude=24.9° and longitude=9.2°) in Mali, on 11/08/2015 at 14UTC. The model PSDs are only from that grid model box interpolated at 1, 2, and 3 km height and for the particular timestep (11/08/2015 at 14UTC). The red squares correspond to the "observed FENNEC-PSD" sorted into the five bins. The error bars provide the maximum and minimum limits of the "observed FENNEC-PSD", sorted into the five model size bins, after including the standard deviation of "observed FENNEC-PSD". The "observed FENNEC-PSD" (see Section 2.2.1) has been derived from several flights above dust sources, thus it is representative of the PSDs above Sahara sources and it used here as reference. The black squares depict the "fitted FENNEC-PSD" sorted into five bins, used in the model parameterization to calculate the emitted dust mass of the corresponding five model transport bins. The difference between the "fitted FENNEC-PSD" and the "fitted FENNEC-PSD" occurs due to the fitting process. The modelled volume concentration is reduced with height by an order of magnitude between 2 and 3 km for particles with diameters 17-40 μm (bin 4). At 3km the simulated concentrations of particles in bin 4 and bin 5 are very low compared to the measurements in Fig. S2a of Ryder et al., (2013a) which indicate the removal of giant particles above 4 km (Ryder et al., 2013a, Figure S2a). Although a direct comparison between the modelled and the observed PSD for this particular emission point is not feasible, since the FENNEC campaign took place on different dates than the AER-D and there are no available measurements above dust sources for the period we performed our simulations, we note a modification of the PSD shape, both for model and observations at 1km. It is evident that the model overestimates the PSD for bins 1-3 while the opposite is found in the size spectrum of the super-coarse (bin4) and giant (bin5) dust particles. Therefore, a model weakness is revealed at the very early phase of the dust transport. Those differences can be attributed to an overestimation of their loss during uplift from the surface to 1 km, or to higher updrafts that remain unresolved in our numerical experiment. Another possible source of this underestimation could be the utilization of a not well-defined PSD shape constraining the distribution of emitted dust mass to the model transport size bins. The use of a PSD with a higher contribution of coarse and giant dust particles could possibly improve the representation of the coarse and giant particles aloft (Fig. S2 and S3) and can be assessed in future studies. Additionally, comparing the "observed FENNEC-PSD" with the modelled PSD of the scenario with the maximum relative reduction of the settling velocities (UR80) in Fig. 5, we find a significant increase of the modelled volume concentrations, reducing the differences seen in volume concentrations in bin4 and bin5 without the reduction of the settling velocity, although the underestimation in bin 5 is still evident.

3.3 Mean dust load

In Fig. 6, the spatial patterns of the columnar dust concentrations are depicted, averaged over the period of 5/8/15-25/8/15, for the total mass as well as for each one of the five size bins simulated with the CONTROL run. Among the first three bins, there are evident many similarities of the dust load spatial features, with maximum values in the Western Sahara whereas the dust advection pathways towards the Atlantic Ocean are clearly seen. In terms of intensity, the mass increases

365 from bin1 to bin 3 (5.5 – 17 μm), yielding the maximum values throughout the size ranges. Dust particles with diameters

366 between 17 μm and 40 μm (bin 4) are found mainly over land, and are subjected to short-range transport westwards (i.e., off

367 the Moroccan coast). Giant particles (bin 5) are found at very low concentrations (< 0.5 gr m^{-2}), at isolated areas over/near dust

368 sources, since the strong impact of gravitational settling prohibits their accumulation and transport.

3.4 Dust size distribution

370 Figure 7 illustrates the simulated PSDs, from each experiment (i.e., CONTROL and URx), along with those acquired

371 by the airborne in situ measurements at different segments and altitudes of the flight b928 in the surrounding area of Cape

372 Verde (downwind region). For the other AER-D flights (i.e., b920, b924, b932 and b934) similar findings are drawn and for

373 brevity reasons are omitted here and are included in the supplementary material (Fig.S4). All AER-D measurements

374 demonstrate the impacts of the processes that are associated with dust transport. The red squares represent the observations

375 and the error bars represent the total (random and systematic) measurement error (see Sect 2.2.1). The modelled PSDs are

376 collocated in space and time with the measurements of each flight segment. For each flight segment, we extract the modeled

377 PSD by interpolating the dust field to the specific altitude of the flight RUN. Additionally, we average the dust field of the

378 nearest grid cell to each coordinate pair along the flight segment track, and the eight neighbouring grid cells of the same

379 altitude. The coordinates of the flight leg track are depicted with orange dots and the collocated grid points used for deriving

380 the modelled PSD (at the specific height of each flight leg) with blue dots. In the time dimension, we average the two hourly

381 model outputs that contain the times of the measurement. In case that the time of measurement coincides with the exact hourly

382 output, the model output on that hour along with the outputs prior and after that are averaged. The error bars in the model PSDs

383 indicate the standard deviation of the collocated grid points averaging in space and time.

384 Based on our findings, for the CONTROL run, the model performs considerably well particularly near the surface

385 and above 4 km, reproducing the volume concentration of the particles residing within bins 1 and 2. Underestimations are

386 found for the third bin with the simulated volume concentration falling however within the measurement uncertainties

387 envelope. As expected, for bins 4 and 5, the model is not capable of reproducing the observed PSD at distant areas since quite

388 significant underestimations have been already notified above sources (see Fig. 5a). The reduction of the settling velocity (i.e.,

389 URx runs, see Table 3) has negligible impact on the level of agreement between model and observations for bins 1 and 2,

390 moderate for bin3 while is determinant for the super-coarse (bin 4) and giant (bin 5) dust particles. Nevertheless, for achieving

391 the best model-observations matching, the necessary reduction (expressed in percentage) on the settling velocity is not constant

392 among the defined transport bins. Focusing on bins 4, the UR60 run (i.e., reduction of the settling velocity by 60%) outperforms

393 the other numerical experiments and focusing on bin 5 the UR80 run.

394 The overall comparison of the observed and modelled average PSDs is presented in Fig 8. We are considering all the

395 in situ airborne measurements and the WRF-L numerical outputs satisfying the defined spatiotemporal collocation criteria.

396 Error bars indicate the corresponding standard deviation. Figure 8a shows that the best model performance is found for the

397 UR80 experiments resembling satisfactory the bin 4 and bin 3/5 concentrations, respectively. These "artificial" reductions

398   translate to settling velocities equal ~0.066 for bin 3 (D=5.5-17 μm), ~0.32 m/s for bin 4 (D=17-40 μm) and ~1.88 m/s for bin

399   5 (D=40-100 μm). it is also reminded that for the same experiment it has been achieved the best agreement against the

400   FENNEC-PSD above dust sources (see Fig. 5 and the relevant discussion).

401   An alternative comparison between observations and model volume concentrations, for the selected AER-D samples

402   (each flight segment is denoted with different marker), has been performed and the obtained results, at each flight altitude, are

403   depicted in Figure 8b. More specifically, we calculate for each model experiment (denoted with different colour), the relative

404   differences (expressed in percentage) of the total dust volume concentration with respect to the in-situ measurements. In

405   addition, the corresponding differences (in percentage terms) that are representative for the altitudes spanning from near-

406   surface up to ~4.2 km are denoted with the vertical coloured dashed thick lines (WRF-L experiments). Those differences are

407   derived by averaging the relative differences of each flight segment. Overall, the model tends to underestimate the total dust

408   volume concentration (relative differences up to 100% in absolute terms) even though occasionally positive departures are

409   found, as indicated by the spread of the individual biases around zero. Nevertheless, the main finding from this analysis is that

410   the model-observation declinations reduce when the settling velocity reduces too (i.e., URx runs). Among the WRF-L

411   experiments, the minimum biases (~5%) are obtained for the UR40 scenario (i.e. the vertical orange dashed line resides close

412   to zero). Through the inspection of the vertically resolved "behavior" of the individual runs, it is revealed that in some cases

413   the model-observation biases can be minimized for the UR60 and UR80 runs and this "variability" highlights the complexity

414   of the underlying mechanisms governing the suspension of airborne dust.

3.5 Dust vertical distribution

416   Figure 9(a) shows the profile of the mean extinction coefficient at 532 nm, provided by the LIVAS pure-dust product

417   (black line), and the profile of the mean extinction coefficients at 550 nm, provided by the CONTROL, UR20, UR40, UR60,

418   and UR80 experiments. The orange area indicates the standard deviation of the LIVAS profiles. Figure9(b) depicts the mean

419   absolute model bias with respect to LIVAS profiles for the different simulations and the vertical dashed lines show the

420   corresponding bias averaged over different altitudes. The mean LIVAS profile is provided by averaging the night-time profiles

421   over the region between 25.5oW to 12.5oE and 11.5oN to 35.5oN, during 5 to 25 August 2015. This area includes the main

422   dust sources that affected the vicinity of Cape Verde (Ryder et al., 2018) and the region of the dust outflow over the Ocean, as

423   well. The nightime profiles excel in accuracy over the daytime ones, due to the lower signal-to-noise ratio (SNR) during the

424   night. The model profiles are collocated in space and time with the LIVAS profiles, as described in Sect. 2.1.4 and the model

425   extinction coefficient is provided with the Eq.13.

426   The intercompared profiles are in good agreement, with the simulations falling well-within the variability of the dust

427   observations, although discrepancies are also present, especially close to the dust sources, in the nighttime boundary layer

428   (Fig.9(b) – region I), and within the upper free Troposphere (Fig. 9(b) – region III). The assessment of the different model

429   experiments against the ESA-LIVAS pure-dust product is performed in the region between 1.5 km and 6.4 km a.m.s.l. (Fig. 9

430   – region II), to avoid possible biases propagating into the analysis (i.e., complex topography and surface returns-region I, SNR

431 and tenuous aerosol layers – region II). According to the comparison of observations and simulations of the mean extinction

432 coefficient (Fig. 9(a)), the statistical overall analysis reveals that the UR40 experiment demonstrates a better performance

433 compared to LIVAS, reducing the mean bias close to zero. For the same experiment the minimum mean bias with respect to

434 the total volume concentration is achieved (see discussion of Fig.9b in Sect. 3.4). However, the UR80 experiment provides a

435 more constant (positive) bias with height, which suggests a better distribution of the dust mass in the vertical.

436 **4 Discussion**

437 The frequent presence of large desert dust particles (D>20 μm) far from their sources, is well established by numerous

438 observational studies over the last decade (van der Does et al., 2018; Liu et al., 2018; Ryder et al., 2013a, 2013b, 2018, 2019a;

439 Weinzierl et al., 2009, 2011, 2017). However, the processes that result in the particle retainment in the atmosphere, and

440 subsequently their travel at greater distances than predicted, remains unrevealed. In this study we extend the particle size range

441 applied in the transport parameterization of the GOCART-AFWA dust scheme of WRF, to include particles with diameters up

442 to 100 μm. The evaluation against airborne in situ observations of the size distribution shows that the concentrations of the

443 larger particles are underestimated, both above dust sources and distant areas. This suggests that there are atmospheric

444 processes that are not taken into account in the model simulations. We investigate the effect of reducing the settling velocity

445 of the dust particles due to these unknown processes, and we see that for a reduction of 60% and (especially for) 80%, the

446 simulations of the PSD in Cape Verde are improved with respect to the observations. The reduction of 80% corresponds to a

447 reduction in settling velocity of 0.0066 m/s for particles with D between 5.5 and 17 μm, which is double than the value reported

448 by Maring et al. (2003) for similar sizes. It should be noted though that Maring et al. (2003) derived this settling velocity using

449 observations that were taken with a five-year difference. Ginoux (2003), has also reported an improvement in model

450 simulations for a reduction in settling velocity of approximately 45% and 60%, for particles with diameters 10 to 30 μm.

451 Though, the differences in the model resolution, the dust scheme and the drag coefficient in Ginoux (2003) compared to this

452 study, could cause the different values of the required corrections in the settling velocities. The difference with the values

453 suggested herein, can mainly be attributed to the different drag coefficient used in Ginoux (2003), which results in lower

454 settling velocities for the spherical particles. Meng et al. (2022) performed a study, similar to this, where after reducing the

455 settling velocity by 13% for accounting for particles' asphericity based on Huang et al., (2020), performed sensitivity tests

456 reducing the dust particles' density from 2500 kg m^{-3} to 1000, 500, 250 and 125 kg m^{-3}. They found that a decrease in the

457 modelled dust aerosol density by 10-20 times its physical value (2500 kg m^{-3}) is needed to improve the comparison between

458 the model and the long-range dust observations of coarse particles. A 10 times reduction in particles' density is almost equal

459 to a 90% reduction in the settling velocity (starting from the Clift and Gauvin (1971) drag coefficients and assuming conditions

460 of U.S. Standard Atmosphere, Fig. S1). It is clear that a huge reduction in the settling velocity in both the Meng et al., (2022)

461 methodology and this work is required, although the physical processes occurring to explain this reduction are not clear.

462   One of the processes proposed in the literature to explain the longer atmospheric lifetimes of large mineral dust
463   particles is the particle asphericity. Ginoux (2003) compared randomly-oriented prolate spheroids and spheres of the same
464   cross section. They showed that spheroids fall slightly slower than their spherical counterparts, with their difference being
465   negligible for spheroids with aspect ratio values less than 5. Huang et al. (2020) compared randomly-oriented ellipsoids and
466   spheres of the same volume. They showed that ellipsoids fall around 20% slower than spheres. Mallios et al. (2020) compared
467   prolate spheroids and spheres of the same maximum dimension, and of the same volume. Moreover, they did not assume
468   randomly-oriented particles, but particles of specific orientation (horizontal and vertical). They showed that the results of the
469   comparison change when the maximum dimension or the volume-equivalent size is used in the comparison. Prolate spheroids,
470   with aspect ratio values in the range of 1.4-2.4, fall slower than spheres of the same maximum dimension, regardless of
471   orientation, with the relative difference between the settling velocities reaching the value of 52%. On the other hand, prolate
472   spheroids, in the same aspect ratio value range, fall faster than spheres of the same volume, regardless of orientation. The
473   comparison with in situ observations of the maximum dimension of particles is not so common, since most of the in-situ
474   measurements do not provide the sizing of the particles in terms of their maximum dimension, with some exceptions, as e.g.
475   the observations shown in van der Does et al. (2016) of individual giant mineral particles (larger than 100 μm in maximum
476   dimension).

477   All the above show that more work is needed for the definite and accurate quantification of the particle asphericity
478   effect on their settling. Nevertheless, there are indications pointing that aspherical particles remain in the atmosphere longer,
479   and that asphericity can be one of the reasons for the differences between the modelling results and the observations.

480   Another process that can influence mineral dust settling has to do with the electrical properties of dust particles. The
481   dust particles are charged in the atmosphere either due to the attachment of atmospheric ions on them (Mallios et al. 2021b)
482   or/and due to collisions, a process known as triboelectric effect (Ette, 1971, Eden and Vonnegut, 1973, Mills, 1977, Jayaratne,
483   1991, Mallios et al., 2022). Moreover, there is a large-scale atmospheric electric field, due to the potential difference between
484   the lower part of the Ionosphere and the Earth's surface (Rycroft et al., 2008). The electric field is modified by ion attachment
485   process (Mallios et al. 2021b) or by the charge separation caused by updrafts (Krauss et al., 2003). Therefore, electrical forces
486   are generated that might influence the particle settling process by balancing the gravity or changing the particle orientation.
487   The quantification of the particles' electrical properties is still an open question

488   Another possible source of error in the gravitational losses simulated by the model as proposed by (Ginoux, 2003) is
489   the numerical diffusion in the advection equation of gravitational settling. Since in the GOCART-AFWA dust scheme of WRF
490   (and WRF-L) a first-order upwind scheme is adapted for the gravitational losses, which is rather diffusive (Versteeg and
491   Malalasekera, 2007), an investigation of the possible improvement on the results by the replacement of the scheme with a less
492   diffusive would be of interest. A possible limitation of this study is the accuracy of the PSD which is used for the distribution
493   on the model transport bins of the emitted fluxes. The simplification in the assumption that the shape of the PSD at 1km above
494   the sources remains unchanged in lower heights near the ground, could possibly introduce errors in the representation of the
495   presence of dust particles aloft.

496   In any case, the proposed scheme presented here, provides a useful tool for the investigation of the physical processes

497   in the transport of coarse and giant particles, along with their impacts on other physical processes in the atmosphere, such as

498   ice nucleation and radiation interactions. The artificial reduction in the settling velocity is not attributed to a known physical

499   mechanism (although results from the past literature reveal some candidates that can give results on the same order of

500   magnitude). Thus, despite the encouraging results, more research is needed towards understanding the physical or numerical

501   processes driving this finding, including the estimation of the impact of non-spherical particles, electricity, the radiation impact

502   on thermodynamics and the disturbance of the mass balance due to the numerical diffusion.

5 Summary and conclusions

503

504   In the current state-of-the-art atmospheric dust models, several physical processes governing dust life cycle

505   components are not well represented or they are not included in the relevant parameterization schemes. This drawback, along

506   with the lack of knowledge on the underlying mechanisms, results in the failure of the numerical simulations to reproduce

507   adequately the long-range transport of super-coarse and giant mineral particles, as it has been justified via their evaluation

508   versus sophisticated dust observations. Among the model limitations, well documented in literature, one of the critical is the

509   neglect of mineral particles with diameters larger than 20 μm, under the erroneous assumption that they deposit quickly after

510   their emission.

511   In the current study, we modify the transport particle size distribution in WRF, expanding at size ranges up to 100

512   μm in diameter, by constraining the shape of the modelled PSD with the observed one above dust sources, acquired in the

513   framework of the FENNEC 2011 campaign. A novelty of our work constitutes the upgrade of the drag coefficient, determining

514   the settling velocity of dust particles, for accounting realistic dust particles sizes ($Re < 10^5$), opposite to what is assumed in the

515   traditional Stokes' theory. After optimally tuning the CONTROL run, we performed a series of sensitivity experiments in

516   which the settling velocity has been reduced, aiming to artificially resemble the real forces acting on particles moving vertically

517   and counteract gravitational settling. Our period of interest spans from 5th to 25th August 2015, when the AER-D campaign

518   took place in the surrounding area of Cape Verde, residing in the core of the "corridor" of the Saharan dust transport along the

519   Tropical Atlantic Ocean. In our experiments, the simulation domain covers most of the Sahara Desert (encompassing the most

520   active dust sources worldwide) and the eastern sector of the Tropical Atlantic Ocean (receiving large amounts of mineral

521   particles from the nearby Saharan dust sources). The dust-related numerical outputs produced by the CONTROL and URx

522   (referring to the reduction of the settling velocity by 20%, 40%, 60% and 80% and it is expressed by the term x) experiments

523   are evaluated against the LIVAS satellite datasets providing pure dust extinction vertical profiles. Nevertheless, special

524   attention is given on the evaluation of the WRF-L PSD against airborne in-situ measurements acquired in the framework of

525   the AER-D campaign.

526   Based on our results, in the CONTROL experiment, the model tends to underestimate the dust volume concentration

527   of coarse and giant dust particles (FENNEC) since the very early stage of dust transport, when the emitted mineral particles

are uplifted at 1 km above the sources. Subsequently, the initially obtained model underestimation becomes more pronounced, against those measured in AER-D, particularly for the super-coarse (bin 4, diameters from 17 to 40 μm) and giant (bin 5, diameters from 40 to 100 μm) dust particles, in the vicinity of Cape Verde (i.e., downwind region). Our findings are in line with the already stated underestimation of the presence of coarse and giant dust particles' presence during their long range dust transport. Nevertheless, when we gradually reduce the settling velocity (URx runs) the model performance steadily improves. Overall, among the numerical experiments, the best match of the simulated and the observed PSDs is achieved for the UR80 scenario (i.e., reduction of the settling velocity by 80%), thus highlighting the misrepresentation or the absence of forces, within the model parameterization schemes, acting on dust particles and counteract gravitational settling. Through the case-by-case inspection, it is revealed that the UR60 and UR40 scenarios can also occasionally provide the optimum model-observations agreement thus highlighting the complexity of the real physical processes that regulate dust particles' settling velocity and suspension. From the evaluation of the vertically resolved simulated dust extinction against the corresponding measurements from the LIVAS dataset, it is revealed that for the UR40 run the model-observations are minimized (oscillating around zero) whereas the UR80 run outperforms in reproducing the vertical structure of the dust layers within the Saharan Air Layer. Summarizing, our work demonstrated an innovative approach in order to overcome existing drawbacks of the atmospheric-dust models towards improving the simulations of dust transport along the Tropical Atlantic Ocean. There are several candidate mechanisms, along with inappropriate definition and treatment of mineral particles in the parameterization schemes, hampering models in reproducing adequately the observed dust patterns. Despite our encouraging results, there are many mandatory steps towards upgrading the current state-of-the-art atmospheric dust models in anticipation of an optimum assessment of the multifaceted role of dust aerosols within the Earth-Atmosphere system.

Author Contributions: ED, VA, and AT design the study; SM guided ED on the methodology for the replacement of the drag coefficient. AT provided useful assistance on the treatment of airborne observations. CR provided the data from the airborne in situ measurements and provided useful information about the instrumentation methods. ED developed the code, performed the simulations and analyzed the results. AG and CR consulted ED on the methodology of in situ and WRF datasets. VA, EM and EP provided the LIVAS dataset, lead the collocation methodology and helped on the interpretation of the results. ED plotted the model and observation data (apart from LIVAS). EP treated and plotted LIVAS data; ED wrote the manuscript draft; VA, AT, AG, EP, SM, CS, SS, EM, CR, DB and PK provided critical feedback and reviewed and edited the manuscript.

Funding: This research was supported by the project "PANhellenic infrastructure for Atmospheric Composition and climatE change" (no. MIS 5021516), which is implemented under the action "Reinforcement of the Research and Innovation Infrastructure", funded by the "Competitiveness, Entrepreneurship and Innovation" Operational Programme (NSRF 2014–2020) and co-financed by Greece and the European Union (European Regional Development Fund). Support was also provided by D-TECT (Grant Agreement 725698) funded by the European Research Council (ERC). ED would like to acknowledge funding by Greece and the Stavros Niarhos Foundation (SNF). CLR was funded by NERC grant reference NE/M018288/1.

562 EM was funded by the European Research Council
563 661 (grant no. 725698, D-TECT) and by a DLR VO-R young investigator group and the Deutscher Akademischer
564 Austauschdienst (grant no. 57370121). AG acknowledges support by the Hellenic Foundation for Research and Innovation (H.
565 F. R. I.) under the "2nd Call for H. F. R. I. Research Projects to support Post-Doctoral Researchers" (project acronym:
566 ATLANTAS, project number: 544).

567

568 **Acknowledgements:** This work was supported by computational time granted from the National Infrastructures for Research
569 and Technology S.A. (GRNET S.A.) in the National HPC facil–ty - A–IS - under project ID pa210502-TRAP-P. We thank the
570 PANhellenic GEophysical observatory of Antikythera (PANGEA) for providing access to the LIVAS data used in this study
571 and their computational center. The National Centers for Environmental Prediction (NCEP) is gratefully acknowledged for the
572 provision of the Global Forecasting System (GFS) operational analyses and the real time global (RTG) sea surface temperature
573 (SST) analyses. We would like to thank the NASA CALIPSO team and NASA/LaRC/ASDC for making the CALIPSO
574 products available, which have been used to build the LIVAS products, and ESA, who funded the LIVAS project (contract no.
575 4000104106/11/NL/FF/fk).

576

577 **Data Availability:** The model outputs and the data used for the analysis are available upon request from Vassilis Amiridis
578 (vamoir@noa.gr) and/or Eleni Drakaki (eldrakaki@noa.gr). The LIVAS dust products are available upon request from Vassilis
579 Amiridis (vamoir@noa.gr), Emmanouil Proestakis (proestakis@noa.gr), and/or Eleni Marinou (elmarinou@noa.gr).

580

581 **Code Availability:** The source code of WRF-L is available upon request from Vassilis Amiridis (vamoir@noa.gr) and/or Eleni
582 Drakaki (eldrakaki@noa.gr).

583 **References**

584 Amiridis, V., Wandinger, U., Marinou, E., Giannakaki, E., Tsekeri, A., Basart, S., Kazadzis, S., Gkikas, A., Taylor, M.,
585 Baldasano, J. and Ansmann, A.: Optimizing CALIPSO Saharan dust retrievals, Atmos. Chem. Phys., 13(23), 12089–12106,
586 doi:10.5194/acp-13-12089-2013, 2013.

587 Amiridis, V., Marinou, E., Tsekeri, A., Wandinger, U., Schwarz, A., Giannakaki, E., Mamouri, R., Kokkalis, P., Binietoglou,
588 I., Solomos, S., Herekakis, T., Kazadzis, S., Gerasopoulos, E., Proestakis, E., Kottas, M., Balis, D., Papayannis, A., Kontoes,
589 C., Kourtidis, K., Papagiannopoulos, N., Mona, L., Pappalardo, G., Le Rille, O. and Ansmann, A.: LIVAS: a 3-D multi-
590 wavelength aerosol/cloud database based on CALIPSO and EARLINET, Atmos. Chem. Phys., 15(13), 7127–7153,
591 doi:10.5194/acp-15-7127-2015, 2015.

592   Basart, S., Vendrell, L. and Baldasano, J. M.: High-resolution dust modelling over complex terrains in West Asia, Aeolian
593   Res., 23, 37–50, doi:10.1016/j.aeolia.2016.09.005, 2016.

594   Bullard, J. E., Baddock, M., Bradwell, T., Crusius, J., Darlington, E., Gaiero, D., Gassó, S., Gisladottir, G., Hodgkins, R.,
595   McCulloch, R., McKenna-Neuman, C., Mockford, T., Stewart, H. and Thorsteinsson, T.: High-latitude dust in the Earth
596   system, Rev. Geophys., 54(2), 447–485, doi:10.1002/2016RG000518, 2016.

597   Chimot, J., Pepijn Veefkind, J., Vlemmix, T., De Haan, J. F., Amiridis, V., Proestakis, E., Marinou, E. and Levelt, P. F.: An
598   exploratory study on the aerosol height retrieval from OMI measurements of the 477 nmO2 O2 spectral band using a neural
599   network approach, Atmos. Meas. Tech., 10(3), 783–809, doi:10.5194/amt-10-783-2017, 2017.

600   Cowie, S. M., Knippertz, P. and Marsham, J. H.: A climatology of dust emission events from Northern Africa using long-term
601   surface observations, Atmos. Chem. Phys., 14(16), 8579–8597, doi:10.5194/acp-14-8579-2014, 2014.

602   Clift, R. and Gauvin, W. H.: Motion of entrained particles in gas streams, Can. J. Chem. Eng., 49(4), 439–448,
603   doi:10.1002/cjce.5450490403, 1971.

604   Clift, R., Grace, J. R. and Weber, M. E.: Bubbles, Drops, and Particles, Dover Publications. [online] Available from:
605   https://books.google.gr/books?id=UUrOmD8niUQC, 2005.

606   Danielson, J. J. and Gesch, D. B.: Global multi-resolution terrain elevation data 2010 (GMTED2010), Open-File Report,
607   https://doi.org/10.3133/ofr20111073, 2011.

608   Daskalopoulou, V., Mallios, S. A., Ulanowski, Z., Hloupis, G., Gialitaki, A., Tsikoudi, I., Tassis, K. and Amiridis, V.: The
609   electrical activity of Saharan dust as perceived from surface electric field observations, Atmos. Chem. Phys., 21(2), 927–949,
610   545 doi:10.5194/acp-21-927-2021, 2021.

611   Davies, C. N.: Definitive equations for the fluid resistance of spheres, Proc. Phys. Soc., 57(4), 259–270, doi:10.1088/0959-
612   5309/57/4/301, 1945.

613   Diehl, K., Debertshäuser, M., Eppers, O., Schmithüsen, H., Mitra, S. K. and Borrmann, S.: Particle surface area dependence
614   of mineral dust in immersion freezing mode: Investigations with freely suspended drops in an acoustic levitator and a vertical
615   wind tunnel, Atmos. Chem. Phys., 14(22), 12343–12355, doi:10.5194/acp-14-12343-2014, 2014.

616   van der Does, M., Knippertz, P., Zschenderlein, P., Giles Harrison, R. and Stuut, J. B. W.: The mysterious long-range transport
617   of giant mineral dust particles, Sci. Adv., 4(12), eaau2768, doi:10.1126/sciadv.aau2768, 2018.

618   Du, Y., Xu, X., Chu, M., Guo, Y. and Wang, J.: Air particulate matter and cardiovascular disease: The epidemiological,
619   biomedical and clinical evidence, J. Thorac. Dis., 8(1), E8–E19, doi:10.3978/j.issn.2072-1439.2015.11.37, 2016.

620 Dubovik, O., Holben, B. N., Lapyonok, T., Sinyuk, A., Mishchenko, M. I., Yang, P. and Slutsker, I.: Non-spherical aerosol
621 retrieval method employing light scattering by spheroids, Geophys. Res. Lett., 29(10), 54-1-54–4, doi:10.1029/2001gl014506,
622 2002.

623 Eden, H. F. and Vonnegut, B.: Electrical Breakdown Caused by Dust Motion in Low-Pressure Atmospheres: Considerations
624 for Mars, Science (80-.)., 180(4089), 962–963, doi:10.1126/science.180.4089.962, 1973.

625 Escribano, J., Tomaso, E. Di, Jorba, O., Klose, M., Ageitos, M. G., Macchia, F., Amiridis, V., Baars, H., Marinou, E.,
626 Proestakis, E., Urbanneck, C., Althausen, D., Bühl, J., Mamouri, R. and García-pando, C. P.: Assimilating spaceborne lidar
627 dust extinction improves dust forecasts, , (June), 1–36, 2021.

628 Ette, A. I. I.: The effect of the Harmattan dust on atmospheric electric parameters, J. Atmos. Terr. Phys., 33(2), 295–300,
629 doi:https://doi.org/10.1016/0021-9169(71)90208-X, 1971.

630 Garcia-Carreras, L., Parker, D. J., Marsham, J. H., Rosenberg, P. D., Brooks, I. M., Lock, A. P., Marenco, F., Mcquaid, J. B.
631 and Hobby, M.: The turbulent structure and diurnal growth of the Saharan atmospheric boundary layer, J. Atmos. Sci., 72(2),
632 693–713, doi:10.1175/JAS-D-13-0384.1, 2015.

633 Gasteiger, J., Groß, S., Sauer, D., Haarig, M., Ansmann, A. and Weinzierl, B.: Particle settling and vertical mixing in the
634 Saharan Air Layer as seen from an integrated model, lidar, and in situ perspective, Atmos. Chem. Phys., 17(1), 297–311,
635 doi:10.5194/acp-17-297-2017, 2017.

636 Gelaro, R., McCarty, W., Suárez, M. J., Todling, R., Molod, A., Takacs, L., Randles, C. A., Darmenov, A., Bosilovich, M. G.,
637 Reichle, R., Wargan, K., Coy, L., Cullather, R., Draper, C., Akella, S., Buchard, V., Conaty, A., da Silva, A. M., Gu, W., Kim,
638 G. K., Koster, R., Lucchesi, R., Merkova, D., Nielsen, J. E., Partyka, G., Pawson, S., Putman, W., Rienecker, M., Schubert, S.
639 D., Sienkiewicz, M. and Zhao, B.: The modern-era retrospective analysis for research and applications, version 2 (MERRA-
640 2), J. Clim., 30(14), 5419–5454, doi:10.1175/JCLI-D-16-0758.1, 2017.

641 Georgoulias, A. K., Alexandri, G., Kourtidis, K. A., Lelieveld, J. and Zanis, P.: Spatiotemporal variability and contribution of
642 different aerosol types to the aerosol optical depth over the Eastern Mediterranean, , 13853–13884, doi:10.5194/acp-16-13853-
643 2016, 2016.

644 Georgoulias, A. K., Tsikerdekis, A., Amiridis, V., Marinou, E., Benedetti, A., Zanis, P., Alexandri, G., Mona, L., Kourtidis,
645 K. A. and Lelieveld, J.: A 3-D evaluation of the MACC reanalysis dust product over Europe, northern Africa and Middle East
646 using CALIOP/CALIPSO dust satellite observations, Atmos. Chem. Phys., 18(12), 8601–8620, doi:10.5194/acp-18-8601-
647 2018, 2018.

648 Georgoulias, A. K., Boersma, K. F., Van Vliet, J., Zhang, X., Van Der A, R., Zanis, P. and De Laat, J.: Detection of NO2
649 pollution plumes from individual ships with the TROPOMI/S5P satellite sensor, Environ. Res. Lett., 15(12), doi:10.1088/1748-
650 9326/abc445, 2020.

Giannadaki, D., Pozzer, A. and Lelieveld, J.: Modeled global effects of airborne desert dust on air quality and premature mortality, Atmos. Chem. Phys., 14(2), 957–968, doi:10.5194/acp-14-957-2014, 2014.

Giles, D. M., Sinyuk, A., Sorokin, M. G., Schafer, J. S., Smirnov, A., Slutsker, I., Eck, T. F., Holben, B. N., Lewis, J. R., Campbell, J. R., Welton, E. J., Korkin, S. V. and Lyapustin, A. I.: Advancements in the Aerosol Robotic Network (AERONET) Version 3 database - Automated near-real-time quality control algorithm with improved cloud screening for Sun photometer aerosol optical depth (AOD) measurements, Atmos. Meas. Tech., 12(1), 169–209, doi:10.5194/amt-12-169-2019, 2019.

Gilliam, R. C. and Pleim, J. E.: Performance Assessment of New Land Surface and Planetary Boundary Layer Physics in the WRF-ARW, J Appl Meteorol Climatol, 49, 760–774, https://doi.org/10.1175/2009JAMC2126.1, 2010.

Ginoux, P., Chin, M., Tegen, I., Goddard, T. and In-, G.: Sources and distributions of dust aerosols simulated with the GOCART model, J. Geophys. Res., 106, 20255–20273, 2001.

Ginoux, P.: Effects of nonsphericity on mineral dust modeling, J. Geophys. Res., 108(D2), doi:10.1029/2002jd002516, 2003.

Ginoux, P., Prospero, J. M., Gill, T. E., Hsu, N. C. and Zhao, M.: Global-scale attribution of anthropogenic and natural dust sources and their emission rates based on MODIS Deep Blue aerosol products, Rev. Geophys., 50(3), 1–36, doi:10.1029/2012RG000388, 2012.

Gkikas, A., Proestakis, E., Amiridis, V., Kazadzis, S., Di Tomaso, E., Tsekeri, A., Marinou, E., Hatzianastassiou, N. and Pérez Garciá-Pando, C.: ModIs Dust AeroSol (MIDAS): A global fine-resolution dust optical depth data set, Atmos. Meas. Tech., 14(1), 309–334, doi:10.5194/amt-14-309-2021, 2021.

Gkikas, A., Proestakis, E., Amiridis, V., Kazadzis, S., Di Tomaso, E., Marinou, E., Hatzianastassiou, N., Kok, J. F. and García-Pando, C. P.: Quantification of the dust optical depth across spatiotemporal scales with the MIDAS global dataset (2003-2017), Atmos. Chem. Phys., 22(5), 3553–3578, doi:10.5194/acp-22-3553-2022, 2022.

Gliß, J., Mortier, A., Schulz, M., Andrews, E., Balkanski, Y., Bauer, S. E., Benedictow, A. M. K., Bian, H., Checa-Garcia, R., Chin, M., Ginoux, P., Griesfeller, J. J., Heckel, A., Kipling, Z., Kirkeväg, A., Kokkola, H., Laj, P., Le Sager, P., Tronstad Lund, M., Lund Myhre, C., Matsui, H., Myhre, G., Neubauer, D., Van Noije, T., North, P., Olivié, D. J. L., Rémy, S., Sogacheva, L., Takemura, T., Tsigaridis, K. and Tsyro, S. G.: AeroCom phase III multi-model evaluation of the aerosol life cycle and optical properties using ground- And space-based remote sensing as well as surface in situ observations, Atmos. Chem. Phys., 21(1), 87–128, doi:10.5194/acp-21-87-2021, 2021.

Goudie, A. S.: Desert dust and human health disorders, Environ. Int., 63, 101–113, doi:10.1016/j.envint.2013.10.011, 2014.

Goudie, A. S. and Middleton, N. J.: Desert Dust in the Global System., 2006.

Grell, G. A. and Dévényi, D.: A generalized approach to parameterizing convection combining ensemble and data assimilation techniques, Geophys Res Lett, 29, 10–13, https://doi.org/10.1029/2002GL015311, 2002.

681 Grell, G. A., Peckham, S. E., Schmitz, R., McKeen, S. A., Frost, G., Skamarock, W. C. and Eder, B.: Fully coupled "online"
682 chemistry within the WRF model, Atmos. Environ., 39(37), 6957–6975, doi:10.1016/j.atmosenv.2005.04.027, 2005.

683 Gu, Z., He, Y., Zhang, Y., Su, J., Zhang, R., Yu, C. W. and Zhang, D.: An overview of triggering mechanisms and
684 characteristics of local strong sandstorms in china and haboobs, Atmosphere (Basel)., 12(6), 1–17,
685 doi:10.3390/atmos12060752, 2021.

686 Hansen, J. E. and Travis, L. D.: Light scattering in planetary atmospheres, Space Sci. Rev., 16(4), 527–610,
687 doi:10.1007/BF00168069, 1974.

688 Harb, K., Butt, O., Abdul-jauwad, S. and Al-yami, A. M.: Systems Adaptation for Satellite Signal under Dust , Sand and
689 Gaseous Attenuations, J. Wirel. Netw. Commun., 3(3), 39–49, doi:10.5923/j.jwnc.20130303.03, 2013.

690 Heinold, B., Tegen, I., Esselborn, M., Kandler, K., Knippertz, P., Müller, D., Schladitz, A., Tesche, M., Weinzierl, B.,
691 Ansmann, A., Althausen, D., Laurent, B., Massling, A., Müller, T., Petzold, A., Schepanski, K. and Wiedensohler, A.: Regional
692 Saharan dust modelling during the SAMUM 2006 campaign, Tellus, Ser. B Chem. Phys. Meteorol., 61(1), 307–324,
693 doi:10.1111/j.1600-0889.2008.00387.x, 2009.

694 Hilsenrath, J. and of Standards, U. S. N. B.: Tables of Thermal Properties of Gases: Comprising Tables of Thermodynamic
695 and Transport Properties of Air, Argon, Carbon Dioxide, Carbon Monoxide, Hydrogen, Nitrogen, Oxygen, and Steam, U.S.
696 Department of Commerce, National Bureau of Standards. [online] Available from:
697 https://books.google.gr/books?id=LK8vaddchE4C, 1955.

698 Huang, Y., Kok, J. F., Kandler, K., Lindqvist, H., Nousiainen, T., Sakai, T., Adebiyi, A. and Jokinen, O.: Climate Models and
699 Remote Sensing Retrievals Neglect Substantial Desert Dust Asphericity, Geophys. Res. Lett., 47(6), 1–11,
700 doi:10.1029/2019GL086592, 2020,

701 Huneeus, N., Schulz, M., Balkanski, Y., Griesfeller, J., Prospero, J., Kinne, S., Bauer, S., Boucher, O., Chin, M., Dentener, F.,
702 Diehl, T., Easter, R., Fillmore, D., Ghan, S., Ginoux, P., Grini, A., Horowitz, L., Koch, D., Krol, M. C., Landing, W., Liu, X.,
703 Mahowald, N., Miller, R., Morcrette, J.-J., Myhre, G., Penner, J., Perlwitz, J., Stier, P., Takemura, T. and Zender, C. S.: Global
704 dust model intercomparison in AeroCom phase I, Atmos. Chem. Phys., 11(15), 7781–7816, doi:10.5194/acp-11-7781-2011,
705 2011.

706 Jayaratne, E. R.: Charge separation during the impact of sand on ice and its relevance to theories of thunderstrom electrification,
707 Atmos. Res., 26(5), 407–424, doi:https://doi.org/10.1016/0169-8095(91)90061-Z, 1991.

708 Jennings, S. G.: The mean free path in air, J. Aerosol Sci., 19(2), 159–166, doi:10.1016/0021-8502(88)90219-4, 1988.

709 Jickells, T. D., An, Z. S., Andersen, K. K., Baker, A. R., Bergametti, C., Brooks, N., Cao, J. J., Boyd, P. W., Duce, R. A.,
710 Hunter, K. A., Kawahata, H., Kubilay, N., LaRoche, J., Liss, P. S., Mahowald, N., Prospero, J. M., Ridgwell, A. J., Tegen, I.

711 and Torres, R.: Global iron connections between desert dust, ocean biogeochemistry, and climate, Science (80-.)., 308(5718),
712 67–71, doi:10.1126/science.1105959, 2005.

713 Jickells, T., Boyd, P. and Hunter, K. A.: Biogeochemical Impacts of Dust on the Global Carbon Cycle, in Mineral Dust: A
714 Key Player in the Earth System, edited by P. Knippertz and J.-B. W. Stuut, pp. 359–384, Springer Netherlands, Dordrecht.,
715 2014.

716 Kandler, K., et al.: Size distribution, mass concentration, chemical and mineralogical composition and derived optical
717 parameters of the boundary layer aerosol at Tinfou, Morocco, during SAMUM 2006, Tellus B, 61, 32–50,
718 https://doi.org/10.1111/j.1600-0889.2008.00385.x, 2009.

719 Knippertz, P. and Stuut, J. B. W.: Mineral dust: A key player in the earth system, Miner. Dust A Key Play. Earth Syst., 1–509,
720 doi:10.1007/978-94-017-8978-3, 2014.

721 Kok, J. F.: An improved parameterization of wind-blown sand flux on Mars that includes the effect of hysteresis, Geophys.
722 Res. Lett., 37(12), doi:10.1029/2010GL043646, 2010.

723 Kok, J. F.: A scaling theory for the size distribution of emitted dust aerosols suggests climate models underestimate the size
724 of the global dust cycle, Proc. Natl. Acad. Sci. U. S. A., 108(3), 1016–1021, doi:10.1073/pnas.1014798108, 2011.

725 Kok, J. F., Adebiyi, A. A., Albani, S., Balkanski, Y., Checa-Garcia, R., Chin, M., Colarco, P. R., Hamilton, D. S., Huang, Y.,
726 Ito, A., Klose, M., Leung, D. M., Li, L., Mahowald, N. M., Miller, R. L., Obiso, V., Pérez García-Pando, C., Rocha-Lima, A.,
727 Wan, J. S. and Whicker, C. A.: Improved representation of the global dust cycle using observational constraints on dust
728 properties and abundance, Atmos. Chem. Phys., 21(10), 8127–8167, doi:10.5194/acp-21-8127-2021, 2021.

729 Konsta, D., Binietoglou, I., Gkikas, A., Solomos, S., Marinou, E., Proestakis, E., Basart, S., García-Pando, C. P., El-Askary,
730 H. and Amiridis, V.: Evaluation of the BSC-DREAM8b regional dust model using the 3D LIVAS-CALIPSO product, Atmos.
731 Environ., 195, 46–62, doi:10.1016/j.atmosenv.2018.09.047, 2018.

732 Kosmopoulos, P. G., Kazadzis, S., El-Askary, H., Taylor, M., Gkikas, A., Proestakis, E., Kontoes, C. and El-Khayat, M. M.:
733 Earth-observation-based estimation and forecasting of particulate matter impact on solar energy in Egypt, Remote Sens.,
734 10(12), 1–23, doi:10.3390/rs10121870, 2018.

735 Krauss, C. E., Horányi, M. and Robertson, S.: Experimental evidence for electrostatic discharging of dust near the surface of
736 Mars, New J. Phys., 5, doi:10.1088/1367-2630/5/1/370, 2003.

737 LeGrand, S. L., Polashenski, C., Letcher, T. W., Creighton, G. A., Peckham, S. E. and Cetola, J. D.: The AFWA dust emission
738 scheme for the GOCART aerosol model in WRF-Chem v3.8.1, Geosci. Model Dev., 12(1), 131–166, doi:10.5194/gmd-12-
739 131-2019, 2019.

740 Li, J. and Osada, K.: Preferential settling of elongated mineral dust particles in the atmosphere, , 34, 17807,
741 doi:10.1029/2007GL030262, 2007.

742 Liu, D., Taylor, J. W., Crosier, J., Marsden, N., Bower, K. N., Lloyd, G., Ryder, C. L., Brooke, J. K., Cotton, R., Marenco, F.,
743 Blyth, A., Cui, Z., Estelles, V., Gallagher, M., Coe, H. and Choularton, T. W.: Aircraft and ground measurements of dust
744 aerosols over the west African coast in summer 2015 during ICE-D and AER-D, Atmos. Chem. Phys., 18(5), 3817–3838,
745 doi:10.5194/acp-18-3817-2018, 2018.

746 Loth, E.: Drag of non-spherical solid particles of regular and irregular shape, Powder Technol., 182(3), 342–353,
747 doi:10.1016/j.powtec.2007.06.001, 2008.

748 Mahowald, N., Albani, S., Kok, J. F., Engelstaeder, S., Scanza, R., Ward, D. S. and Flanner, M. G.: The size distribution of
749 desert dust aerosols and its impact on the Earth system, Aeolian Res., 15, 53–71, doi:10.1016/j.aeolia.2013.09.002, 2014.

750 Mallios, S. A., Drakaki, E. and Amiridis, V.: Effects of dust particle sphericity and orientation on their gravitational settling
751 in the earth's atmosphere, J. Aerosol Sci., 150(April), 105634, doi:10.1016/j.jaerosci.2020.105634, 2020.

752 Mallios, S. A., Papangelis, G., Hloupis, G., Papaioannou, A., Daskalopoulou, V. and Amiridis, V.: Modeling of Spherical Dust
753 Particle Charging due to Ion Attachment, Front. Earth Sci., 9(August), 1–22, doi:10.3389/feart.2021.709890, 2021a.

754 Mallios, S. A., Daskalopoulou, V. and Amiridis, V.: Orientation of non spherical prolate dust particles moving vertically in
755 the Earth's atmosphere, J. Aerosol Sci., 151(November 2019), 105657, doi:10.1016/j.jaerosci.2020.105657, 2021b.

756 Mallios, S. A., Daskalopoulou, V. and Amiridis, V.: Modeling of the electrical interaction between desert dust particles and
757 the Earth's atmosphere, J. Aerosol Sci., 165, 106044, doi:https://doi.org/10.1016/j.jaerosci.2022.106044, 2022.

758 Maring, H.: Mineral dust aerosol size distribution change during atmospheric transport, J. Geophys. Res., 108(D19), 8592,
759 doi:10.1029/2002JD002536, 2003.

760 Marinou, E., Amiridis, V., Binietoglou, I., Tsikerdekis, A., Solomos, S., Proestakis, E., Konsta, Di., Papagiannopoulos, N.,
761 Tsekeri, A., Vlastou, G., Zanis, P., Balis, Di., Wandinger, U. and Ansmann, A.: Three-dimensional evolution of Saharan dust
762 transport towards Europe based on a 9-year EARLINET-optimized CALIPSO dataset, Atmos. Chem. Phys., 17(9), 5893–
763 5919, doi:10.5194/acp-17-5893-2017, 2017.

764 Marinou, E., Tesche, M., Nenes, A., Ansmann, A., Schrod, J., Mamali, D., Tsekeri, A., Pikridas, M., Baars, H., Engelmann,
765 R., Voudouri, K. A., Solomos, S., Sciare, J., Groß, S., Ewald, F. and Amiridis, V.: Retrieval of ice-nucleating particle
766 concentrations from lidar observations and comparison with UAV in situ measurements, Atmos. Chem. Phys., 19(17), 11315–
767 11342, doi:10.5194/acp-19-11315-2019, 2019.

Meng, J., Huang, Y., Leung, D. M., Li, L., Adebiyi, A. A., Ryder, C. L., Mahowald, N. M. and Kok, J. F.: Improved Parameterization for the Size Distribution of Emitted Dust Aerosols Reduces Model Underestimation of Super Coarse Dust, Geophys. Res. Lett., 49(8), e2021GL097287, doi:https://doi.org/10.1029/2021GL097287, 2022.

Mie, G.: Beiträge zur Optik trüber Medien, speziell kolloidaler Metallösungen, Ann. Phys., 330(3), 377–445, doi:https://doi.org/10.1002/andp.19083300302, 1908.

Mills, A. A.: Dust clouds and frictional generation of glow discharges on Mars, Nature, 268(5621), 614, doi:10.1038/268614a0, 1977.

Nakanishi, M. and Niino, H.: An improved Mellor-Yamada Level-3 model: Its numerical stability and application to a regional prediction of advection fog, Boundary Layer Meteorol, 119, 397–407, https://doi.org/10.1007/s10546-005-9030-8, 2006.

Nickovic, S., Cvetkovic, B., Petković, S., Amiridis, V., Pejanović, G., Solomos, S., Marinou, E. and Nikolic, J.: Cloud icing by mineral dust and impacts to aviation safety, Sci. Rep., 11(1), 6411, doi:10.1038/s41598-021-85566-y, 2021.

Nicoll, K. A., Harrison, R. G. and Ulanowski, Z.: Observations of Saharan dust layer electrification, Environ. Res. Lett., 6(1), 1–8, doi:10.1088/1748-9326/6/1/014001, 2011.

O'Sullivan, D., Marenco, F., Ryder, C., Pradhan, Y., Kipling, Z., Johnson, B., Benedetti, A., Brooks, M., McGill, M., Yorks, J. and Selmer, P.: Models transport Saharan dust too low in the atmosphere compared to observations, Atmos. Chem. Phys. Discuss., 1–47, doi:10.5194/acp-2020-57, 2020.

Okin, G. S., Mahowald, N., Chadwick, O. A. and Artaxo, P.: Impact of desert dust on the biogeochemistry of phosphorus in terrestrial ecosystems, Global Biogeochem. Cycles, 18(2), doi:10.1029/2003GB002145, 2004.

Pérez, C., Nickovic, S., Pejanovic, G., Baldasano, J. M. and Özsoy, E.: Interactive dust-radiation modeling: A step to improve weather forecasts, J. Geophys. Res., 111(D16), D16206, doi:10.1029/2005JD006717, 2006.

Petters, M. D. and Kreidenweis, S. M.: A single parameter representation of hygroscopic growth and cloud condensation nucleus activity-Part 3: Including surfactant partitioning, Atmos. Chem. Phys., 13(2), 1081–1091, doi:10.5194/acp-13-1081-2013, 2013.

Proestakis, E., Amiridis, V., Marinou, E., Georgoulias, A. K., Solomos, S., Kazadzis, S., Chimot, J., Che, H., Alexandri, G., Binietoglou, I., Daskalopoulou, V., Kourtidis, K. A., De Leeuw, G. and Van Der A, R. J.: Nine-year spatial and temporal evolution of desert dust aerosols over South and East Asia as revealed by CALIOP, Atmos. Chem. Phys., 18(2), 1337–1362, doi:10.5194/acp-18-1337-2018, 2018.

Prospero, J. M., Bonatti, E., Schubert, C. and Carlson, T. N.: Dust in the Caribbean atmosphere traced to an African dust storm, Earth Planet. Sci. Lett., 9(3), 287–293, doi:10.1016/0012-821X(70)90039-7, 1970.

Prospero, J. M., Ginoux, P., Torres, O., Nicholson, S. E. and Gill, T. E.: Environmental characterization of global sources of atmospheric soil dust identified with the Nimbus 7 Total Ozone Mapping Spectrometer (TOMS) absorbing aerosol product, Rev. Geophys., 40(1), 2-1-2–31, doi:10.1029/2000RG000095, 2002.

Renard, J. B., Dulac, F., Durand, P., Bourgeois, Q., Denjean, C., Vignelles, D., Couté, B., Jeannot, M., Verdier, N. and Mallet, M.: In situ measurements of desert dust particles above the western Mediterranean Sea with the balloon-borne Light Optical Aerosol Counter/sizer (LOAC) during the ChArMEx campaign of summer 2013, Atmos. Chem. Phys., 18(5), 3677–3699, doi:10.5194/acp-18-3677-2018, 2018.

Roberts, A. J., Marsham, J. H., Knippertz, P., Parker, D. J., Bart, M., Garcia-Carreras, L., Hobby, M., McQuaid, J. B., Rosenberg, P. D. and Walker, D.: New Saharan wind observations reveal substantial biases in analysed dust-generating winds, Atmos. Sci. Lett., 18(9), 366–372, doi:10.1002/asl.765, 2017.

Rycroft, M. J., Harrison, R. G., Nicoll, K. A. and Mareev, E. A.: An Overview of Earth's Global Electric Circuit and Atmospheric Conductivity, Space Sci. Rev., 137(1), 83–105, doi:10.1007/s11214-008-9368-6, 2008.

Ryder, C. L., Highwood, E. J., Lai, T. M., Sodemann, H. and Marsham, J. H.: Impact of atmospheric transport on the evolution of microphysical and optical properties of Saharan dust, Geophys. Res. Lett., 40(10), 2433–2438, doi:10.1002/grl.50482, 2013a.

Ryder, C. L., Highwood, E. J., Rosenberg, P. D., Trembath, J., Brooke, J. K., Bart, M., Dean, A., Crosier, J., Dorsey, J., Brindley, H., Banks, J., Marsham, J. H., McQuaid, J. B., Sodemann, H. and Washington, R.: Optical properties of Saharan dust aerosol and contribution from the coarse mode as measured during the Fennec 2011 aircraft campaign, Atmos. Chem. Phys., 13(1), 303–325, doi:10.5194/acp-13-303-2013, 2013b.

Ryder, C. L., Marenco, F., Brooke, J. K., Estelles, V., Cotton, R., Formenti, P., McQuaid, J. B., Price, H. C., Liu, D., Ausset, P., Rosenberg, P. D., Taylor, J. W., Choularton, T., Bower, K., Coe, H., Gallagher, M., Crosier, J., Lloyd, G., Highwood, E. J. and Murray, B. J.: Coarse-mode mineral dust size distributions, composition and optical properties from AER-D aircraft measurements over the tropical eastern Atlantic, Atmos. Chem. Phys., 18(23), 17225–17257, doi:10.5194/acp-18-17225-2018, 2018.

Ryder, C. L., Highwood, E. J., Walser, A., Seibert, P., Philipp, A. and Weinzierl, B.: Coarse and giant particles are ubiquitous in Saharan dust export regions and are radiatively significant over the Sahara, Atmos. Chem. Phys., 19(24), 15353–15376, doi:10.5194/acp-19-15353-2019, 2019.

Sanjeevi, S. K. P., Kuipers, J. A. M. and Padding, J. T.: Drag, lift and torque correlations for non-spherical particles from Stokes limit to high Reynolds numbers, Int. J. Multiph. Flow, 106, 325–337, doi:10.1016/j.ijmultiphaseflow.2018.05.011, 2018.

827 Shao, B., Liu, G. R., Lin, T., Xu, G. X. and Yan, X.: Rotation and orientation of irregular particles in viscous fluids using the
828 gradient smoothed method (GSM), Eng. Appl. Comput. Fluid Mech., 11(1), 557–575, doi:10.1080/19942060.2017.1329169,
829 2017.

830 Sinyuk, A., Holben, B. N., Eck, T. F., Giles, D. M., Slutsker, I., Korkin, S., Schafer, J. S., Smirnov, A., Sorokin, M. and
831 Lyapustin, A.: The AERONET Version 3 aerosol retrieval algorithm, associated uncertainties and comparisons to Version 2,
832 Atmos. Meas. Tech., 13(6), 3375–3411, doi:10.5194/amt-13-3375-2020, 2020.

833 Solomos, S., Kallos, G., Kushta, J., Astitha, M., Tremback, C., Nenes, A. and Levin, Z.: An integrated modeling study on the
834 effects of mineral dust and sea salt particles on clouds and precipitation, Atmos. Chem. Phys., 11(2), 873–892,
835 doi:10.5194/acp-11-873-2011, 2011.

836 Solomos, S., Ansmann, A., Mamouri, R. E., Binietoglou, I., Patlakas, P., Marinou, E. and Amiridis, V.: Remote sensing and
837 modelling analysis of the extreme dust storm hitting the Middle East and eastern Mediterranean in September 2015, Atmos.
838 Chem. Phys., 17(6), 4063–4079, doi:10.5194/acp-17-4063-2017, 2017.

839 Solomos, S., Kalivitis, N., Mihalopoulos, N., Amiridis, V., Kouvarakis, G., Gkikas, A., Binietoglou, I., Tsekeri, A., Kazadzis,
840 S., Kottas, M., Pradhan, Y., Proestakis, E., Nastos, P. T. and Marenco, F.: From tropospheric folding to Khamsin and Foehn
841 winds: How atmospheric dynamics advanced a record-breaking dust episode in Crete, Atmosphere (Basel)., 9(7),
842 doi:10.3390/atmos9070240, 2018.

843 Stockdale, A., Krom, M. D., Mortimer, R. J. G., Benning, L. G., Carslaw, K. S., Herbert, R. J., Shi, Z., Myriokefalitakis, S.,
844 Kanakidou, M. and Nenes, A.: Understanding the nature of atmospheric acid processing of mineral dusts in supplying
845 bioavailable phosphorus to the oceans, Proc. Natl. Acad. Sci. U. S. A., 113(51), 14639–14644, doi:10.1073/pnas.1608136113,
846 2016.

847 Tagliabue, A., Bowie, A. R., Boyd, P. W., Buck, K. N., Johnson, K. S. and Saito, M. A.: The integral role of iron in ocean
848 biogeochemistry, Nature, 543(7643), 51–59, doi:10.1038/nature21058, 2017.

849 Tesche, M., Ansmann, A., Müller, D., Althausen, D., Mattis, I., Heese, B., Freudenthaler, V., Wiegner, M., Esselborn, M.,
850 Pisani, G. and Knippertz, P.: Vertical profiling of Saharan dust with Raman lidars and airborne HSRL in southern Morocco
851 during SAMUM, Tellus, Ser. B Chem. Phys. Meteorol., 61(1), 144–164, doi:10.1111/j.1600-0889.2008.00390.x, 2009.

852 Textor, C., Schulz, M., Guibert, S., Kinne, S., Balkanski, Y., Bauer, S., Berntsen, T., Berglen, T., Boucher, O., Chin, M.,
853 Dentener, F., Diehl, T., Easter, R., Feichter, H., Fillmore, D., Ghan, S., Ginoux, P., Gong, S., Grini, A., Hendricks, J., Horowitz,
854 L., Huang, P., Isaksen, I., Iversen, T., Kloster, S., Koch, D., Kirkevåg, A., Kristjansson, J. E., Krol, M., Lauer, A., Lamarque,
855 J. F., Liu, X., Montanaro, V., Myhre, G., Penner, J., Pitari, G., Reddy, S., Seland, Stier, P., Takemura, T. and Tie, X.: Analysis
856 and quantification of the diversities of aerosol life cycles within AeroCom, Atmos. Chem. Phys., 6(7), 1777–1813,
857 doi:10.5194/acp-6-1777-2006, 2006.

858 Toth III, J., Rajupet, S., Squire, H., Volbers, B., Zhou, J., Xie, L., Sankaran, R. M. and Lacks, D.: Electrostatic forces alter
859 particle size distributions in atmospheric dust, Atmos. Chem. Phys. Discuss., 1–14, doi:10.5194/acp-2019-650, 2019.

860 Tsekeri, A., Amiridis, V., Tsichla, M., Fountoulakis, I., Nersesian, A., Proestakis, E., Gkikas, A., Papachristopoulou, K.,
861 Barlakas, V., and Kazadzis, S.:The effect of large dust size on solar radiation fluxes, International Radiation Symposium,
862 Thessaloniki, Greece, 4-8 July 2022.

863 Tsikerdekis, A., Zanis, P., Steiner, A. L., Solmon, F., Amiridis, V., Marinou, E., Katragkou, E., Karacostas, T. and Foret, G.:
864 Impact of dust size parameterizations on aerosol burden and radiative forcing in RegCM4, Atmos. Chem. Phys., 17(2), 769–
865 791, doi:10.5194/acp-17-769-2017, 2017.

866 Twohy, C. H., Kreidenweis, S. M., Eidhammer, T., Browell, E. V., Heymsfield, A. J., Bansemer, A. R., Anderson, B. E., Chen,
867 G., Ismail, S., DeMott, P. J. and Van Den Heever, S. C.: Saharan dust particles nucleate droplets in eastern Atlantic clouds,
868 Geophys. Res. Lett., 36(1), 1–6, doi:10.1029/2008GL035846, 2009.

869 U.S. Standard Atmosphere, 1962, U.S. Government Printing Office, Washington, D.C.,
870 1962,https://www.ngdc.noaa.gov/stp/space-weather/online-publications/miscellaneous/us-standard-atmosphere-1976/us-
871 standard-atmosphere_st76-1562_noaa.pdf

872 Versteeg H. K. & Malalasekera W. (2007).An introduction to computational fluid dynamics : the finite volume method (2nd
873 ed.). Pearson Education.

874 Weinzierl, B., Petzold, A., Esselborn, M., Wirth, M., Rasp, K., Kandler, K., SchüTZ, L., Koepke, P. and Fiebig, M.: Airborne
875 measurements of dust layer properties, particle size distribution and mixing state of Saharan dust during SAMUM 2006, Tellus
876 B Chem. Phys. Meteorol., 61(1), 96–117, doi:10.1111/j.1600-0889.2008.00392.x, 2009.

877 Weinzierl, B., Sauer, D., Esselborn, M., Petzold, A., Veira, A., Rose, M., Mund, S., Wirth, M., Ansmann, A., Tesche, M.,
878 Gross, S. and Freudenthaler, V.: Microphysical and optical properties of dust and tropical biomass burning aerosol layers in
879 the Cape Verde region-an overview of the airborne in situ and lidar measurements during SAMUM-2, Tellus, Ser. B Chem.
880 Phys. Meteorol., 63(4), 589–618, doi:10.1111/j.1600-0889.2011.00566.x, 2011.

881 Weinzierl, B., Sauer, D., Minikin, A., Reitebuch, O., Dahlkötter, F., Mayer, B., Emde, C., Tegen, I., Gasteiger, J., Petzold, A.,
882 Veira, A., Kueppers, U. and Schumann, U.: On the visibility of airborne volcanic ash and mineral dust from the pilot's
883 perspective in flight, Phys. Chem. Earth, 45–46, 87–102, doi:10.1016/j.pce.2012.04.003, 2012.

884 Weinzierl, B., Ansmann, A., Prospero, J. M., Althausen, D., Benker, N., Chouza, F., Dollner, M., Farrell, D., Fomba, W. K.,
885 Freudenthaler, V., Gasteiger, J., Groß, S., Haarig, M., Heinold, B., Kandler, K., Kristensen, T. B., Mayol-Bracero, O. L.,
886 Müller, T., Reitebuch, O., Sauer, D., Schäfler, A., Schepanski, K., Spanu, A., Tegen, I., Toledano, C. and Walser, A.: The

887 Saharan aerosol long-range transport and aerosol-cloud-interaction experiment: Overview and selected highlights, Bull. Am.
888 Meteorol. Soc., 98(7), 1427–1451, doi:10.1175/BAMS-D-15-00142.1, 2017.

889 Winker, D. M., Vaughan, M. A., Omar, A., Hu, Y., Powell, K. A., Liu, Z., Hunt, W. H. and Young, S. A.: Overview of the
890 CALIPSO Mission and CALIOP Data Processing Algorithms, J. Atmos. Ocean. Technol., 26(11), 2310–2323,
891 doi:10.1175/2009JTECHA1281.1, 2009.

892 Zastawny, M., Mallouppas, G., Zhao, F. and van Wachem, B.: Derivation of drag and lift force and torque coefficients for
893 non-spherical particles in flows, Int. J. Multiph. Flow, 39, 227–239, doi:10.1016/j.ijmultiphaseflow.2011.09.004, 2012.

894
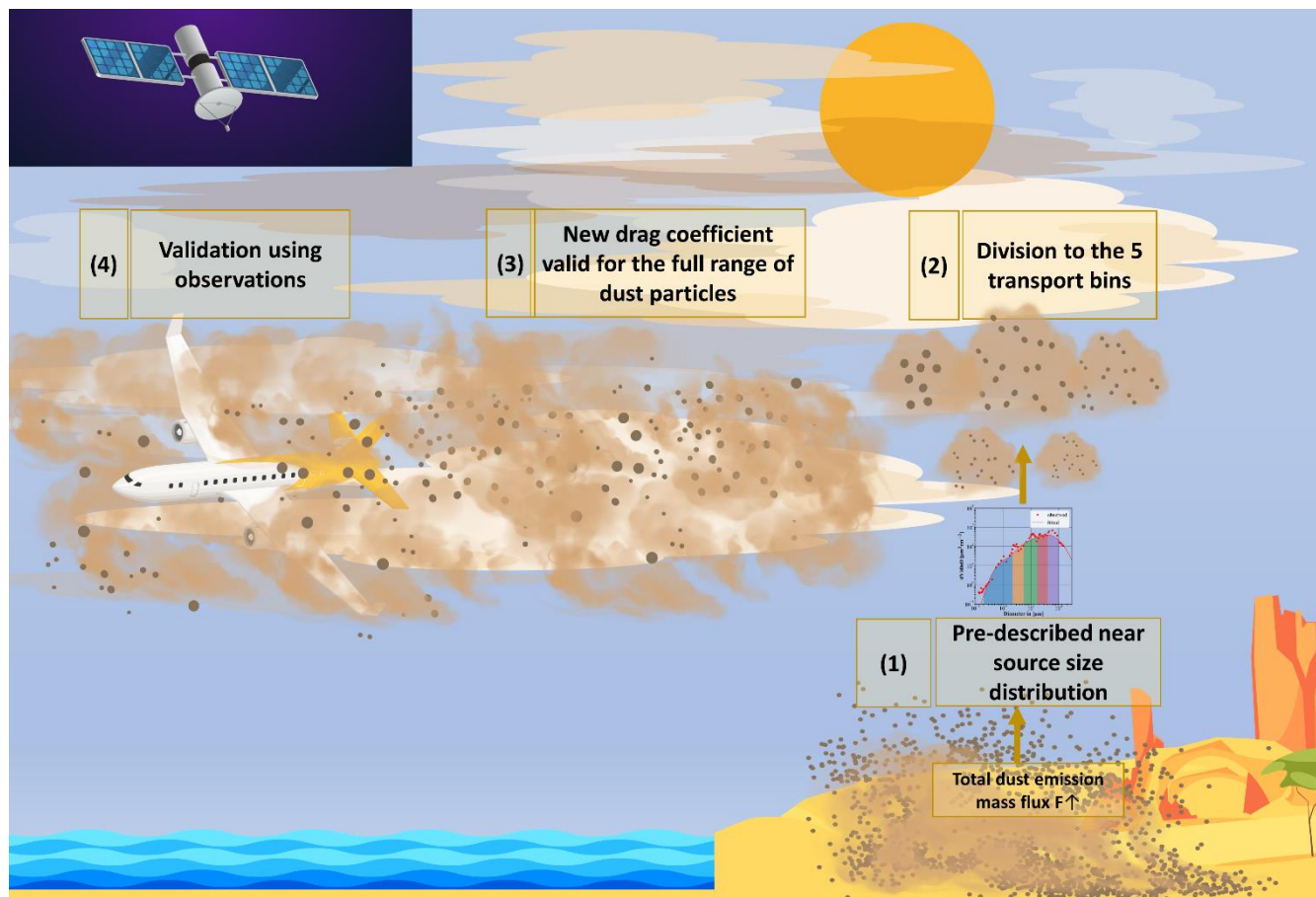
895
896 **Figure 1: The structure of the presented work. Steps (1), (2) and (3) correspond to the appropriate modifications**
897 **implemented in the WRF-Chem GOCART-AFWA dust scheme, for the inclusion of the giant dust particles and the**
898 **development of WRF-L. Step (4) refers to model validation activities.**
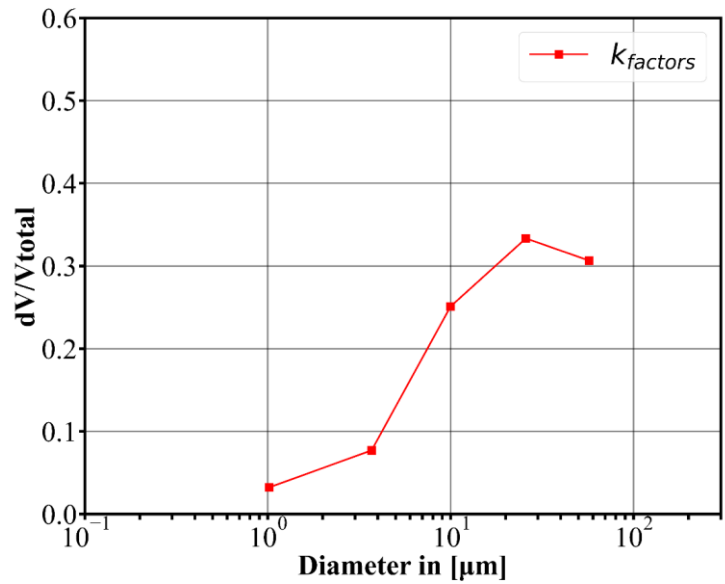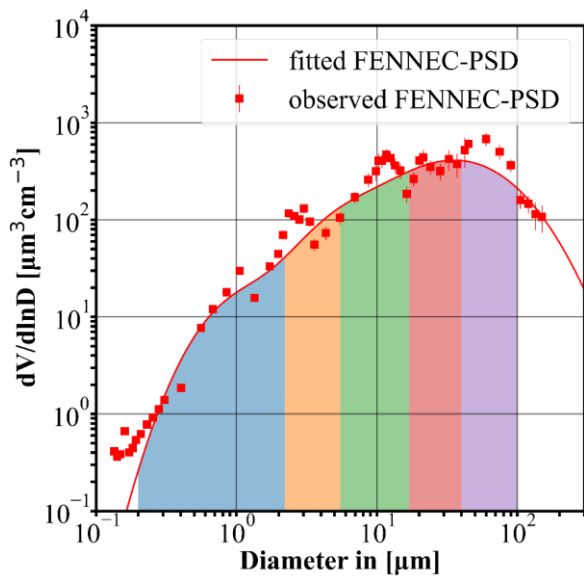
Figure 2: Prescribed dust size distribution used in the WRF-L for the distribution of total dust mass to the transport model size bins: (a) "observed FENNEC-PSD" (µm3cm-3) (red squares), and the respective "fitted FENNEC-PSD" (red solid line). The "observed FENNEC-PSD" corresponds to the PSD observations at 1km, obtained by averaging profile measured data of freshly uplifted dust cases, over 500m. The shaded areas indicate the model transport size bins in WRF-L. Error bars indicate the standard deviation of the observed values (b) The $k_{factors}$ of the transport size bins calculated based on "fitted FENNEC-PSD", provide the mass fraction of the emitted dust for each bin.
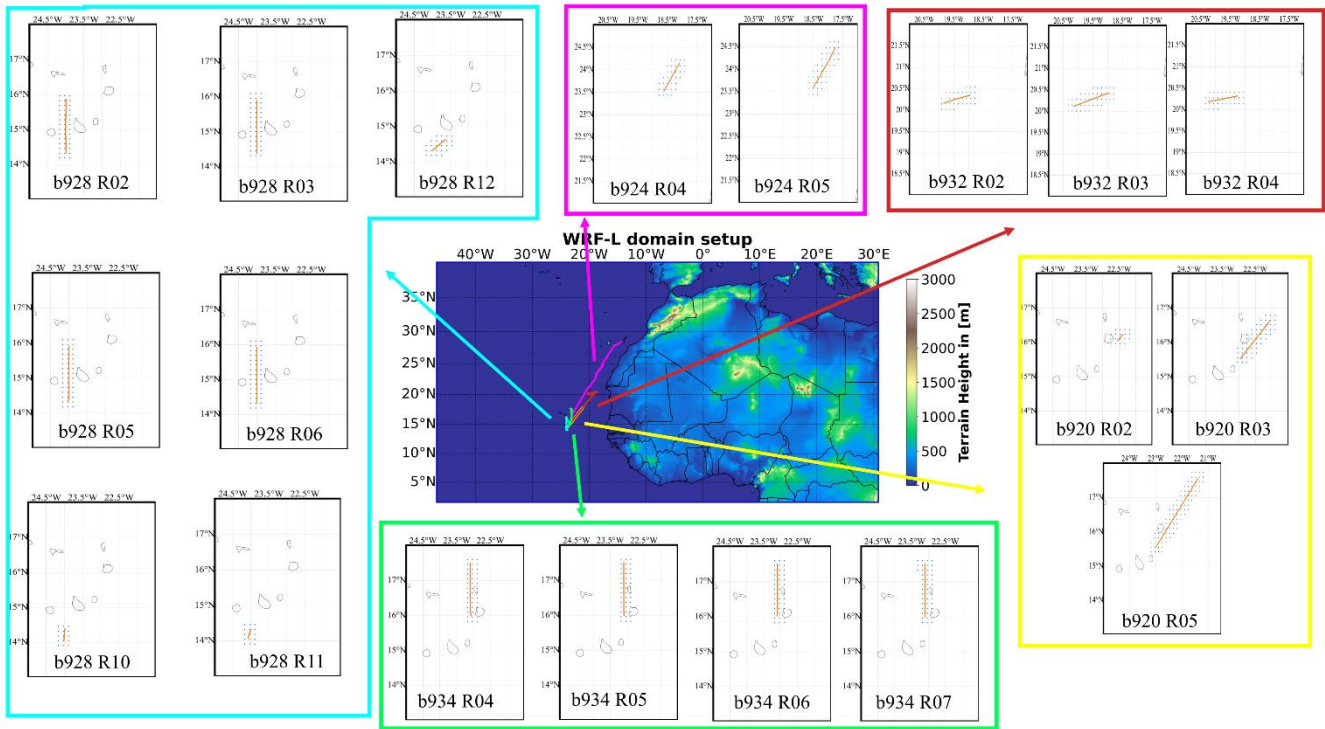
Figure 3: Domain and topography map of the WRF-L model simulations, with a horizontal grid spacing of 15km, and 70 vertical levels. The tracks of the AER-D flights, used in this study (b920, b924, b928, b932 and b934), are depicted in the central plot with different colors. In the surrounding maps, the orange dots indicate the aircraft tracks of each flight RUN. The blue dots correspond to the collocated model grid points.

911
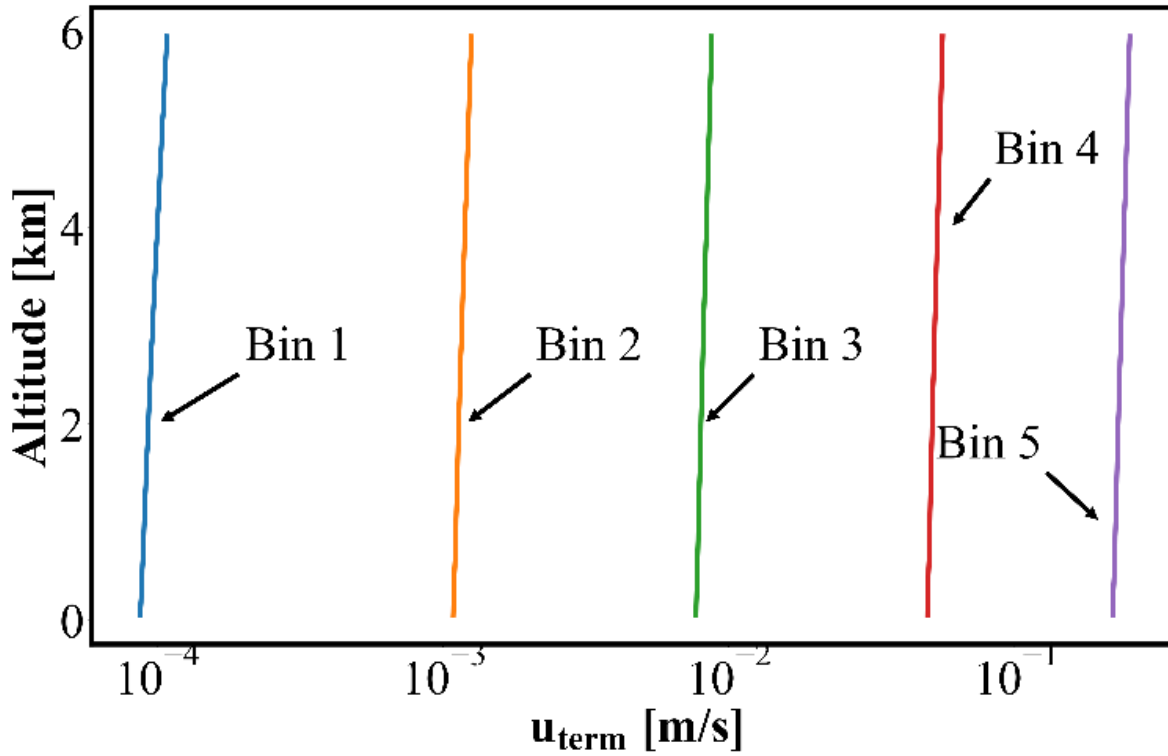
Figure 4: Terminal velocities of the CONTROL experiment, averaged for the simulation time and the domain. Each colored line corresponds to one of the new model size bins, with blue: Bin 1, orange: Bin 2, green: Bin 3, red: Bin 4 and purple: Bin 5.
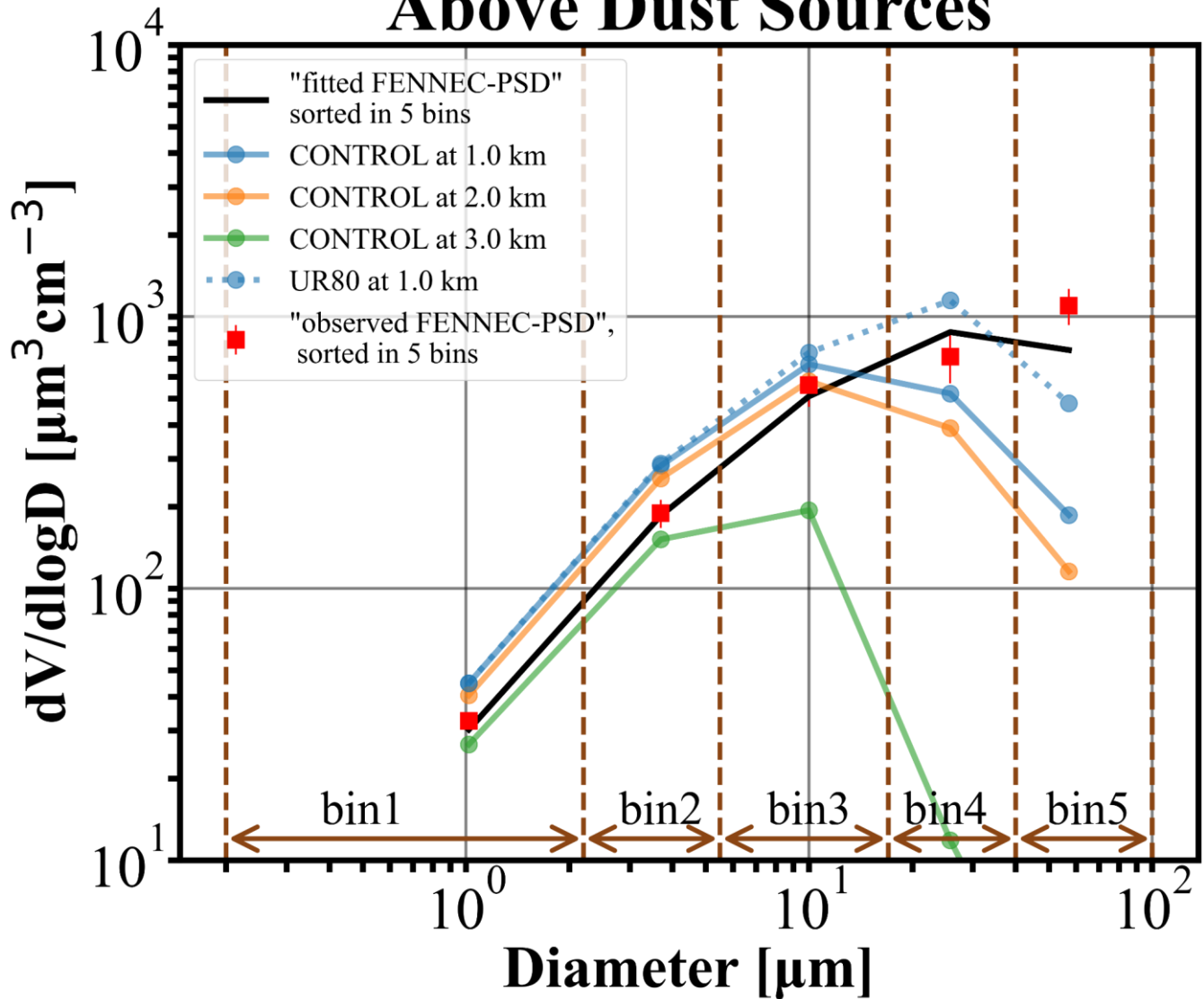
Figure 5: Dust size distribution above an emission model grid point (latitude=24.9o and longitude=9.2o) in Mali, on 11/08/2015 at 14UTC. Blue solid line: the dust PSD of the CONTROL run interpolated at 1 km altitude above the dust source, orange solid line: the dust PSD of the CONTROL run interpolated at 2 km altitude above dust source, green solid line: the dust PSD of the CONTROL run interpolated at 3 km altitude above dust source, blue dotted line: the dust PSD of the UR80 run interpolated at 1 km altitude above the dust source and red squares: the "observed FENNEC-PSD" at 1 km altitude (sorted in 5 bins) , black squares the "fitted FENNEC-PSD" at 1km (sorted in 5 bins) which has been used for the distribution of the model emission to the five size bins.

923
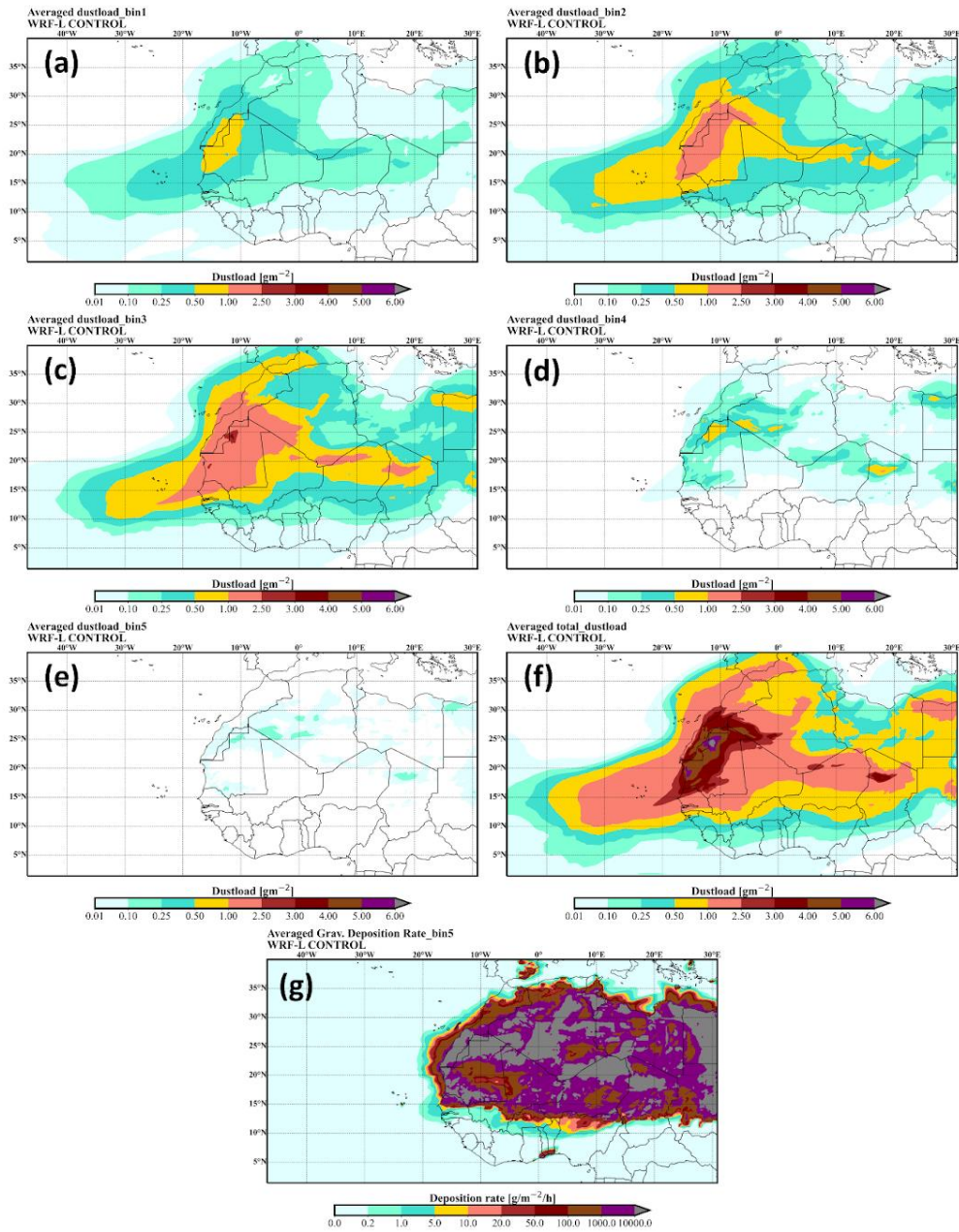
Figure 6: The dust load provided by the model, averaged for the whole simulation period, for (a) bin 1, (b) bin 2, (c) bin 3, (d) bin 4, (e) bin 5, and (f) the whole range of the PSD. The dust load is in g/m². (g) The gravitational deposition rate for bin 5 in g/m²/h.

927
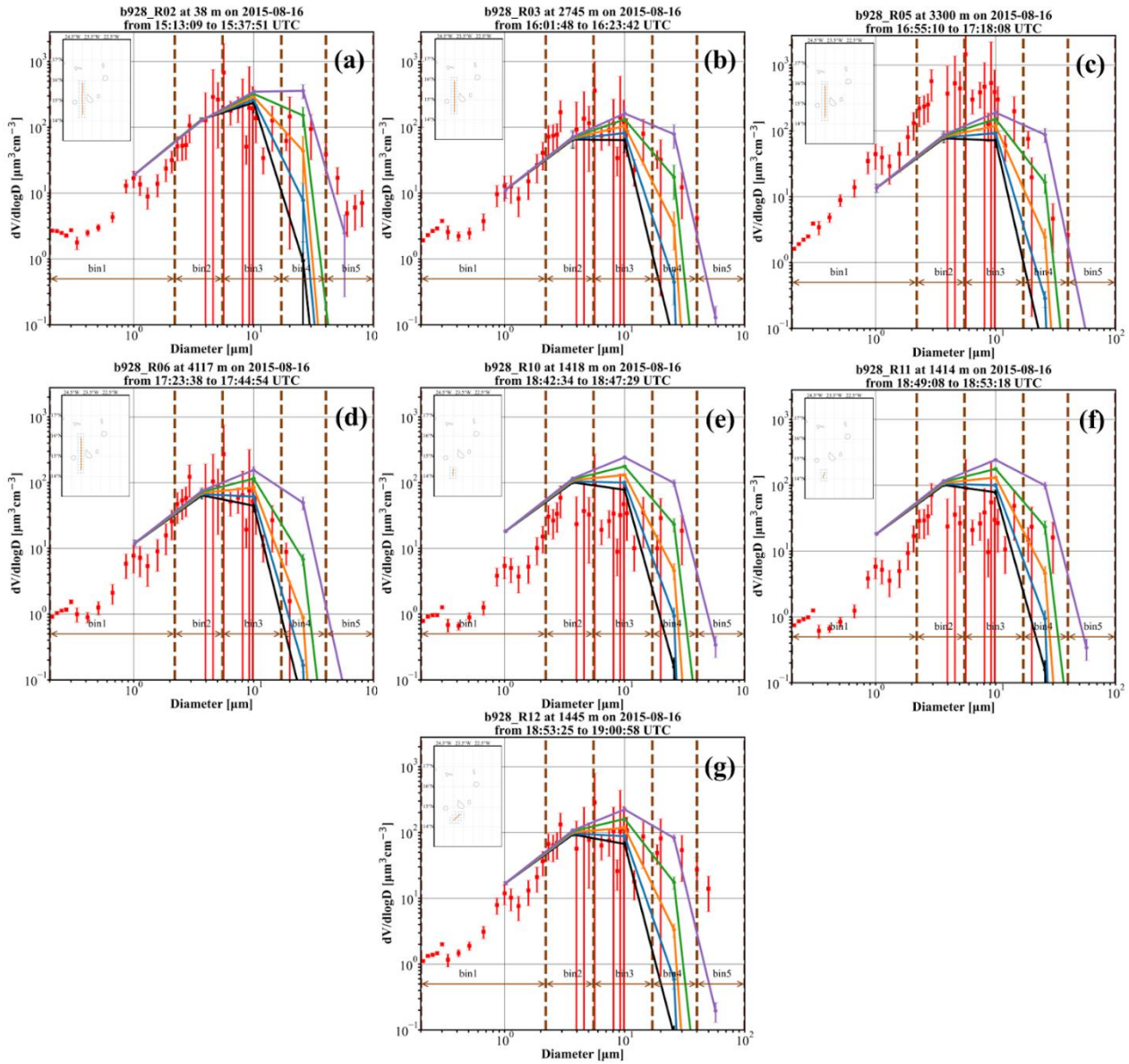
Figure 7: Modeled and observed dust PSD of flight b928, for straight-level-runs (a) R02, (b) R03, (c) R05, (d) R06, (e) R10, (f) R11 and (g) R12. The in situ observations are shown with red squares (along with the total instrumentation error). The collocated modeled PSDs are shown with lines, for the CONTROL run (black), UR20 (blue), UR40 (orange), UR60 (green), and UR80 (purple) and the corresponding standard deviation with the associated error bars. The brown vertical lines indicate the limits of the model size bins. The inlet maps show the flight segment track and the collocated model grid points.
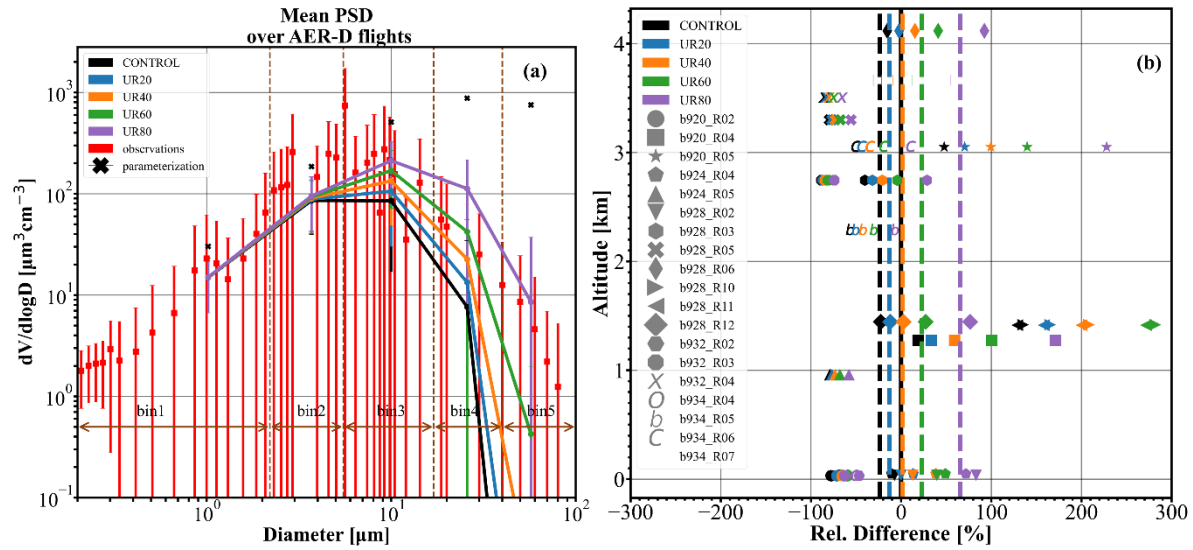
Figure 8: (a) Mean PSD of AER-D/ICE-D campaign. The observations are shown with red squares, whereas the simulations are shown with solid lines for the CONTROL run (black), UR20 (blue), UR40 (orange), UR60 (green), and UR80 (purple). (b) The relative difference between the observations and the model simulations of the total volume of dust particles, at different altitudes. The observations from different flight segments (i.e., b920 R02, b920 R04, b920 R05, b924 R04, b924 R05, b928 R03, b928 R05, b928 R06, b932 R02, b932 R03, b932 R04, b934 R04, b934 R05, b934 R06, and b934 R07) are denoted with different markers. The average relative difference of the observations and the simulations are denoted with dashed lines, for the CONTROL run (black), UR20 (blue), UR40 (orange), UR60 (green), and UR80 (purple).
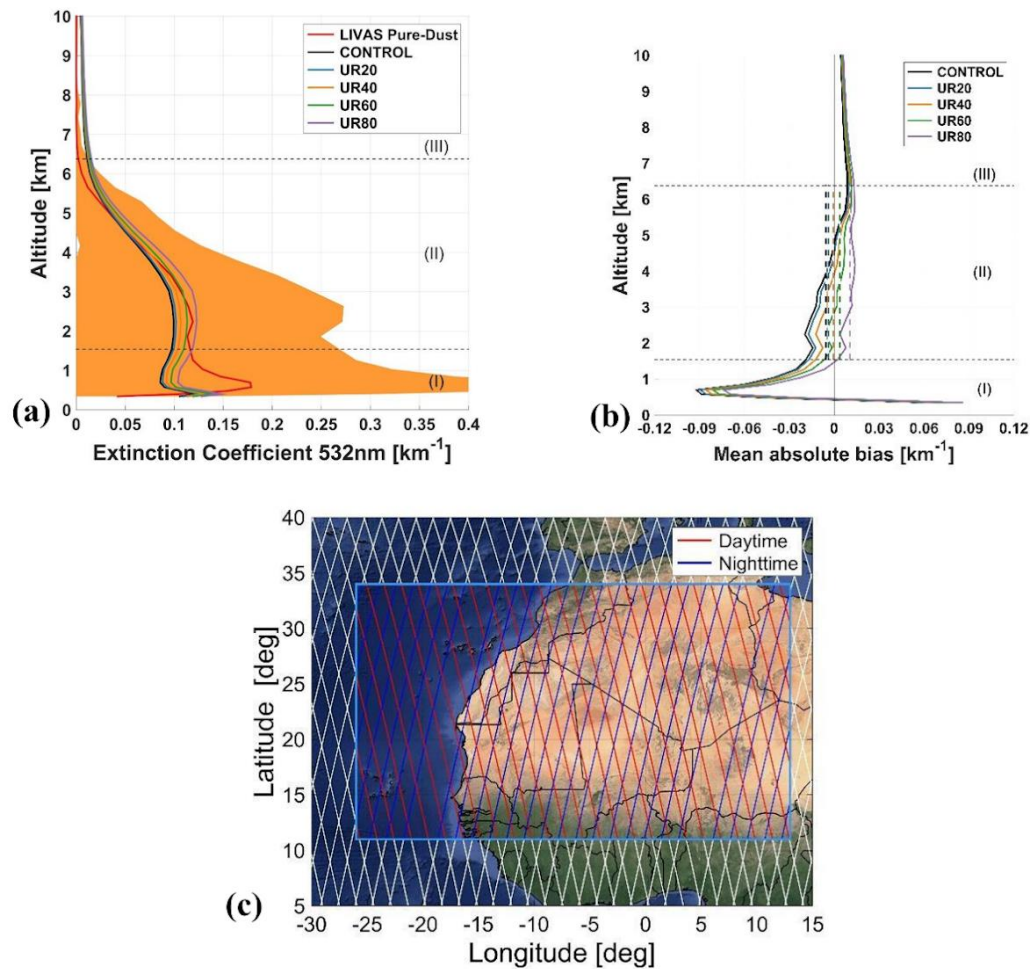
946

947 **Figure 9: (a) Profile of the mean extinction coefficient at 532 nm, by LIVAS pure-dust product (black red line), and**

948 **profiles of the mean extinction coefficient at 532 nm simulated from the different experiments of Table 3 (CONTROL,**

949 **UR20/40/60/80). The orange shading indicates the standard deviation of the LIVAS profile averaging. (b) The mean**

950 **absolute biases between the LIVAS profile and the simulated profiles from the different experiments, in the domain of**

951 **interest, between 05/08/2015 and 25/08/2015. The vertical dashed lines are the mean absolute bias between the LIVAS**

952 **profile and the simulated profiles from the different experiments averaged over the altitudes of region II. (c) The**

953 **domain of interest and the daytime (red) and nighttime (blue) CALIPSO overpasses. The vertical dashed lines are the**

954 **mean absolute bias between the LIVAS profile and the simulated profiles from the different experiments averaged over**

955 **the altitudes of region II.**

956

957

958 **Table 1 Size ranges and properties of model size bins in the default WRF-GOCART-AFWA scheme**

WRF-GOCART-AFWA					
Bins	**1**	**2**	**3**	**4**	**5**
$D_{lo} - D_u$(μm)	0.2-2.0	2.0-3.6	3.6-6.0	6.0-12.0	12.0-20.0
D_{eff} (μm)	1.46	2.8	4.8	9.0	16.0
ρ_p (g cm^{-3})	2.5	2.65	2.65	2.65	2.65
WRF-L					
Bins	**1**	**2**	**3**	**4**	**5**
$D_{lo} - D_u$(μm)	0.2-2.2	2.2-5.5	5.5-17.0	17.0-40.0	40.0-100.0
D_{eff} (μm)	1.02	3.7	10.0	25.8	57.2
ρ_p (g cm^{-3})	2.5	2.65	2.65	2.65	2.65

959

960 **Table 2 Configuration parameters of the WRF-L runs**

Parameterization	Scheme	Parameterization	Scheme
Surface Model	Noah (Chen and Dudhia, 2001)	sf_surface_physics	2
Surface Layer	Monin-Obukov-Janjic (Janić, 2001)	sf_sfclay_physics	2
Radiation (SW and LW)	RRTMG (Iacono et al., 2008)	ra_sw(lw)_physics	4
Microphysics	Morrison 2-moment (Morrison et al., 2005)	mp_physics	10
Cumulus	Grell-3 (Grell and Dévényi, 2002)	cu_physics	5
Boundary Layer	MYNN 2.5 (Nakanishi and Niino, 2006)	bl_pbl_physics	5
Chemistry	GOCART simple (Ginoux et al., 2001; LeGrand et al., 2019)	chem_opt	300
Dust Scheme	AFWA (LeGrand et al., 2019)	dust_opt	3

961 **Table 3 Experimental runs that performed in this study**

Experiment	Code
CONTROL	WRF-L
UR20	WRF-L with reduced settling velocities by 20% of their settling velocity
UR40	WRF-L with reduced settling velocities by 40% of their settling velocity
UR60	WRF-L with reduced settling velocities by 60% of their settling velocity
UR80	WRF-L with reduced settling velocities by 80% of their settling velocity

962 **Table 4: Lognormal ($\frac{dV}{dlnD} = \frac{V_{tot}}{\sqrt{2\pi}ln\sigma_g} exp\left(-\frac{(lnD_v - lnD)^2}{2(ln\sigma_g)^2}\right)$) mode parameters of the fitted FENNEC-PSD. Diameters are**

963 **given in [μm] and volume concentrations in [$\frac{\mu m^3}{cm^3}$]:**

Modes	1	2	3	4	5
V_{tot}	15.16	27.07	169.32	310.5	563.3
D_v	1.0	2.5	7.0	22.0	50.0
s_g	1.8	2.0	1.9	2.0	2.15

964